



Title	Nonmuscle myosin II folds into a 10S form via two portions of tail for dynamic subcellular localization
Author(s)	Kiboku, Takayuki; Katoh, Tsuyoshi; Nakamura, Akio; Kitamura, Akira; Kinjo, Masataka; Murakami, Yota; Takahashi, Masayuki
Citation	Genes to Cells, 18(2), 90-109 https://doi.org/10.1111/gtc.12021
Issue Date	2013-02
Doc URL	http://hdl.handle.net/2115/53054
Rights	The definitive version is available at www3.interscience.wiley.com
Type	article (author version)
Additional Information	There are other files related to this item in HUSCAP. Check the above URL.
File Information	GtC18-2_90-109.pdf



[Instructions for use](#)

Nonmuscle myosin II folds into a 10S form via two portions of tail for dynamic subcellular localization

Takayuki Kiboku,¹ Tsuyoshi Katoh,² Akio Nakamura,³ Akira Kitamura,⁴ Masataka Kinjo,⁴ Yota Murakami,¹ and Masayuki Takahashi,¹

¹Department of Chemistry, Faculty of Science, Hokkaido University, Sapporo, 010-0810, Japan

²Department of Biochemistry, Asahikawa Medical University, Asahikawa, 078-8510, Japan

³Department of Molecular and Cellular Pharmacology, Faculty of Medicine, Gunma University Graduate School of Medicine, Maebashi, 371-8511, Japan

⁴Laboratory of Molecular Cell Dynamics, Faculty of Advanced Life Science, Hokkaido University, Sapporo, 001-0021, Japan

Corresponding author: Masayuki Takahashi,
Department of Chemistry,
Faculty of Science,
Hokkaido University,
Kita-ku Kita 10 Nishi 8, Sapporo, 010-0810, Japan.
Tel: +81-11-706-3814,
Fax: +81-11-706-4924,
E-mail: takahash@sci.hokudai.ac.jp

Running title: Role of 10S form of nonmuscle myosin II

Key words: myosin II, nonmuscle, conformational change, cell migration, cytokinesis

Total characters: 55,938 (including spaces)

Abstract

Nonmuscle myosin II forms a folded conformation (10S form) in the inactivated state; however, the physiological importance of the 10S form is still unclear. To investigate the role of 10S form, we generated a chimeric mutant of nonmuscle myosin IIB (IIB-SK1·2), in which S1462-R1490 and L1551-E1577 were replaced with the corresponding portions of skeletal muscle myosin heavy chain. The IIB-SK1·2 mutant did not fold into a 10S form under physiological condition *in vitro*. IIB-SK1·2 was less dynamic by stabilizing the filamentous form, and accumulated in the posterior region of migrating cells. IIB-SK1·2 functioned properly in cytokinesis, but altered migratory properties; the rate and directional persistence were increased by IIB-SK1·2 expression. Surprisingly, endogenous nonmuscle myosin IIA was excluded from the posterior region of migrating cells expressing IIB-SK1·2, which may underlie the change of the cellular migratory properties. These results suggest that the 10S form is necessary for maintaining nonmuscle myosin II in an unassembled state and for recruitment of nonmuscle myosin II to a specific region of the cell.

Introduction

Nonmuscle myosin II (hereafter, NM-myosin II) is involved in diverse cellular processes, including cell migration (Vicente-Manzanares *et al.* 2009), cytokinesis (Matsumura 2005), and cell-cell adhesion (Conti and Adelstein 2008). NM-myosin II consists of two nonmuscle myosin heavy chains (NMHC), two essential light chains (ELC), and two regulatory light chains (RLC), and is comprised of two globular heads and a long tail. Each globular head can be subdivided into a motor domain, containing an actin-binding site and an ATP-binding site, and a neck domain, containing an ELC-binding site and an RLC-binding site. The tail domain forms an α -helical coiled-coil, rod-like structure and is involved in the assembly of NM-myosin II molecules into filaments.

Together with two pairs of light chains, the three isoforms of mammalian NMHC, NMHC-IIA, NMHC-IIB, and NMHC-IIC, form myosin IIA, IIB, and IIC, respectively (Berg *et al.* 2001; Golomb *et al.* 2004). These three isoforms display distinct kinetic properties (Wang *et al.* 2003; Kovács *et al.* 2003), and genetic ablation in mice suggests functional differences between myosin IIA and IIB (Tullio *et al.* 1997; Conti *et al.* 2004; Wang *et al.* 2010).

NM-myosin II belongs to the class II myosin superfamily, comprising a sarcomeric type (skeletal muscle myosin and cardiac muscle myosin) and a nonsarcomeric type (smooth muscle myosin and NM-myosin II). Sarcomeric myosin is assembled into a thick filament and maintains the sarcomere structure. Although smooth muscle myosin belongs to the nonsarcomeric type, it also forms a filament even in the relaxed state (Somlyo *et al.* 1981). By contrast, NM-myosin II shows a dynamic transition between the monomer and filament states, and this dynamic is regulated spatiotemporally in response to various signals (Vicente-Manzanares *et al.* 2009). To perform the contractile functions with actin filaments, NM-myosin II must assemble into filaments.

Filament formation of nonsarcomeric myosin II is regulated by RLC phosphorylation. Electron microscopic studies revealed that unphosphorylated myosin forms a folded conformation, referred to as the 10S form, based on its sedimentation coefficient, in which the tail bends twice and the second bending site (positioned approximately one-third of the length from the tip of the tail) interacts with the head-tail junction of the myosin molecule (Onishi and Wakabayashi 1982; Trybus *et al.* 1982; Craig *et al.* 1983). Phosphorylation of RLC at Ser19 leads to a conformational change from the 10S form to an extended (unfolded) conformation known as 6S form, which is capable of assembling into filaments (Craig *et al.* 1983; Ikebe *et al.* 1983; Trybus and Lowey 1984). The 10S form traps ADP·Pi tightly and results in almost no ATPase activity (Cross *et al.* 1986). Based on the results of these *in vitro* studies, the 10S form is thought to

function as an “off” state with respect to both motor activity and filament formation in the cell.

To date, most studies investigating the molecular mechanism of the 10S-6S transition have been performed *in vitro* using smooth muscle myosin purified from tissues and reconstituted with RLC mutants (Trybus and Lowey 1988; Ikebe *et al.* 1994). Crosslinking experiments *in vitro* have revealed that RLC interacts with the tail region of the heavy chain when myosin is in the 10S conformation (Olney *et al.* 1996; Salzameda *et al.* 2006), demonstrating that interaction between RLC and specific portions in the myosin tail is critical for folding to a 10S form *in vitro*.

The 10S form was not capable to detect in the relaxed smooth muscle tissue (Somlyo *et al.* 1981; Horowitz *et al.* 1994). However, it was demonstrated that the 10S form of smooth muscle myosin is present in airway smooth muscle cells (Milton *et al.* 2011). A NMHC-IIA mutant lacking the RLC-binding site in the neck domain, which is predicted to destabilize the 10S form, is defective in the regulation of NM-myosin II assembly in living cells, suggesting the presence of a 10S form in the cell (Breckenridge *et al.* 2009). Single molecule negative stain electron microscopy and image processing techniques have revealed the detailed structure of the 10S form of smooth muscle myosin (Burgess *et al.* 2007; Jung *et al.* 2011); a similar structure was also observed for myosin IIA (Jung *et al.* 2008). These findings provide new insights into the conformational change and regulation of nonsarcomeric type myosins (Sellers and Knight 2007; Ikebe 2008; Lowey and Trybus 2010); however, the region in the tail of NM-myosin II that contributes to the 10S form is undetermined. Furthermore, the physiological role of the 10S form of NM-myosin II is still unclear.

In this study, we examined the involvement of the S1462-R1490 and L1551-E1577 regions of NMHC-IIB in folding of myosin IIB into the 10S form, by creating a recombinant chimeric mutant of NMHC-IIB (IIB-SK1·2), in which these regions were replaced with the corresponding regions of skeletal muscle myosin heavy chain. Furthermore, to reveal the role of the 10S form of NM-myosin II in the cell, we examined the behavior of exogenously expressed NMHC-IIB and its effects on cellular motility.

Results

Identification of candidate regions of the myosin IIB tail for formation of 10S form

We attempted to determine which region of the NM-myosin II tail is responsible for formation of the 10S form. Based on the assumption that this region is highly homologous among nonsarcomeric myosin II heavy chains (*MYH9*, *MYH10*, *MYH11*, and *MYH14*) and less homologous to sarcomeric myosin heavy chains (*MYH1*, *MYH6*, and *MYH7*), we searched for candidate regions consisting of approximately 28 amino acid residues (repeating unit length observed in the coiled-coil of myosin II tail) within amino acids 1401–1700 of NMHC-IIB (*MYH10*), which includes the RLC-interacting region (Salzameda *et al.* 2006). Three regions of NMHC-IIB, S1462-R1490, L1551-E1577, and E1588-A1617, named regions 1, 2, and 3, respectively, were identified as potential candidates (Fig. S1). We constructed chimeric NMHC-IIBs (IIB-SK1, IIB-SK2, and IIB-SK3), in which the regions 1, 2, and 3 of NMHC-IIB were replaced with the corresponding regions of skeletal muscle myosin heavy chain (*MYH1*). We also constructed IIB-SK1·2 and IIB-SK1·3, in which the regions 1 and 2, or the regions 1 and 3, were replaced (Fig. 1A).

We assessed the ability of the chimeric NMHC-IIB mutants fused with enhanced green fluorescent protein (EGFP) to associate with the actin cytoskeleton in the cell, using a Triton X-100 solubility assay, in which filamentous NM-myosin II associated with the actin cytoskeleton separates into the insoluble fraction, and monomeric NM-myosin II separates into the soluble fraction. With the exception of IIB-SK1·2, approximately 25% of each myosin IIB mutant was extracted in the soluble fraction. A similar percentage of wild-type myosin IIB (IIB-WT) was also extracted in the soluble fraction, whereas only 8% of IIB-SK1·2 was extracted in this fraction (Fig. 1B,C). We then compared the subcellular localization of chimeric myosin IIBs with that of IIB-WT-fused with mCherry. Four of the five chimeric myosin IIBs, IIB-SK1, IIB-SK2, IIB-SK3, and IIB-SK1·3, were completely colocalized with IIB-WT at the stress fiber-like structure (Fig. 1D). Conversely, IIB-SK1·2 showed distinct localization from IIB-WT; it localized at one side of the cell remarkably (Fig. 1D). The histogram of the ratio of the localized area size of the EGFP-IIB-SK1·2 to that of mCherry-IIB-WT indicates the biased localization of IIB-SK1·2 clearly (Fig. 1E). These results indicate that compared with IIB-WT, IIB-SK1·2 displays distinct behaviors, including differential solubility and subcellular localization in the cell, suggesting that IIB-SK1·2 lacks some aspects of normal NM-myosin II dynamics, and that the region 1 (S1462-R1490) and region 2 (L1551-E1577) of NMHC-IIB are candidate regions for the formation of 10S form.

Two regions of myosin IIB are responsible for formation of the 10S form

To confirm whether regions 1 and 2 are responsible for the formation of a 10S form, we observed the conformation of recombinant IIB-SK1·2 by electron microscopy. Full-length IIB-SK1·2 and IIB-WT were prepared using a baculovirus-insect cell expression system (Fig. 2A). The RLCs of both recombinant NM-myosin IIs were unphosphorylated (Fig. 2B). In agreement with the previously reported disruption of the 10S form of smooth muscle myosin under high salt conditions *in vitro* (Onishi and Wakabayashi 1982; Trybus *et al.* 1982), we observed that the majority of both IIB-WT and IIB-SK1·2 had an extended conformation under high salt conditions (Fig. 2C,F). Similar to purified nonsarcomeric myosin II (Kendrick-Jones *et al.* 1987), a large proportion of IIB-WT molecules were folded into the 10S form under physiological ionic-strength (low salt) conditions in the presence of Mg-ATP (Fig. 2D,E), whereas the majority of IIB-SK1·2 molecules formed a filament structure under the same conditions, even though their RLCs were unphosphorylated (Fig. 2G). The mean length of the IIB-SK1·2 filaments was 375 ± 24 nm ($n = 48$), which is comparable to the length of platelet NM-myosin II filaments reconstituted *in vitro* (Niederman and Pollard 1975). As expected, monomers of IIB-SK1·2 displayed an extended conformation under low salt conditions (Fig. 2H). We classified the observed NM-myosin II molecules into three conformational states: a filamentous form, an extended monomer, and a folded monomer. We then counted the number of molecules belonging to each state, assuming that one filament consists of 28 NM-myosin II molecules, as demonstrated previously (Niederman and Pollard 1975) and in the current study (Fig. 2G). The data demonstrate that IIB-WT exists as a 10S form under low salt conditions, whereas IIB-SK1·2 exists as a filamentous form under the same conditions (Fig. 2I), indicating that IIB-SK1·2 is unable to fold into the 10S form, and forms a filament even in the resting state.

We then examined whether IIB-SK1·2 fused with EGFP is unable to fold into a 10S form. Fluorescence correlation spectroscopy (FCS), which can measure the diffusion state of fluorescent molecules in solution with single molecule sensitivity, was employed to analyze the conformation of EGFP-fused myosin IIBs. We hypothesized that NM-myosin II forming a compact 10S form would diffuse more rapidly throughout the cell than NM-myosin II forming an extended conformation. To inhibit the formation of insoluble filamentous structures of IIB-SK1·2 (as seen in Fig. 2G), which would not be appropriate for FCS measurement in solution, we constructed a charge-reversal mutant of IIB-SK1·2 (IIB-SK1·2-P1m) within the P1 cluster, which is one of the critical regions for assembly (Nakasawa *et al.* 2005). Myosin IIB carrying mutation (K1842E, R1845E, and R1846E), IIB-P1m, was shown to be distributed diffusely throughout the cell (M. Takahashi *et al.*, unpublished data, and also shown in Fig. 4G). Lysates from cells expressing EGFP-IIB constructs (EGFP-IIB-SK1·2-P1m, EGFP-IIB-P1m, and EGFP-IIB-WT), or from control cells

expressing EGFP, were measured by FCS, and normalized autocorrelation functions were determined (Fig. 3A). The autocorrelation functions were fitted with a single-component model and the diffusion times were obtained (Fig. 3B). To emphasize whether the diffusion times are changed in different salt concentration, diffusion times of EGFP-IIBs were normalized to those of EGFP at each salt condition (Fig. 3C). Normalized diffusion times of both IIB-WT and IIB-P1m under high salt conditions were longer than those under low salt conditions. However, normalized diffusion times of IIB-SK1·2-P1m under both conditions were similar, and were comparable to those of IIB-WT and IIB-P1m under high salt conditions. These results suggest that the FCS method is capable of distinguishing between the different conformations of NM-myosin II molecules; such that a shorter diffusion time reflects the 10S form, and a longer diffusion time reflects the extended conformation. Indeed, EGFP-IIB-SK1·2-P1m forms an extended conformation under low salt conditions. The electron microscopy and FCS data imply that the region 1 (S1462-R1490) and region 2 (L1551-E1577) of NMHC-IIB are responsible for the formation of the 10S configuration.

Stabilization of the filamentous form renders IIB-SK1·2 less dynamic

To assess the dynamic properties of IIB-SK1·2 in living cells in more detail, we performed fluorescence recovery after photobleaching (FRAP) analysis using MRC-5 SV1 TG1 cells coexpressing EGFP-IIB-SK1·2 and mCherry-IIB-WT. In almost all photobleached areas, IIB-SK1·2 recovered more slowly than IIB-WT; the half-recovery times for IIB-SK1·2 and IIB-WT were 94 ± 26 s and 64 ± 16 s, respectively (Video S1, Fig. 4A-C). When calculated at each spot independently, the ratio of half-recovery times for IIB-SK1·2 to that for IIB-WT was 1.58 ± 0.56 . These results indicate that IIB-SK1·2 is less dynamic than IIB-WT.

To further assess the behavior of IIB-SK1·2 on the thick fiber structure close to the plasma membrane by more direct imaging, we performed photoconversion analysis using IIB-WT and IIB-SK1·2 tagged with monomeric Kikume Green-Red (mKikGR), which is a photoconvertible fluorescent protein that changes from green to red upon exposure to ultraviolet light (Habuchi *et al.* 2008). Photoconverted (red) IIB-WT disappeared from the fiber structure, and also spread laterally in the fiber structure (or returned from the cytoplasm) during the 60 min period after photoconversion (Video S2 and S3, Fig. 4D-F). Conversely, photoconverted IIB-SK1·2 did not display the same degree of spread on the fiber structure, and the fluorescence intensity did not change during the 60 min period after photoconversion (Video S2 and S3, Fig. 4D-F). These results indicate that IIB-SK1·2 is more stably incorporated into the cytoskeleton and is less dynamic than IIB-WT.

To investigate the behavior of unassembled mutants, we examined the subcellular localization of the charge-reversal mutant of IIB-SK1·2 (IIB-SK1·2-P1m). As expected, EGFP-IIB-P1m was diffusely distributed in the cytoplasm (Fig. 4G). Similarly, mCherry-IIB-SK1·2-P1m, which possibly exists as a monomer forming an extended conformation, was also diffusely distributed (Fig. 4G). Together with the results of the Triton solubility assay (Fig. 1B,C), these results suggest that compared with IIB-WT, the mutations within IIB-SK1·2 shift the monomer-filament equilibrium toward the filamentous state.

IIB-SK1·2 accumulates in the posterior region of migrating cells

Since the NMHC-IIA mutant lacking the RLC-binding domain (Δ IQ2) accumulates in the posterior region of migrating cells (Breckenridge *et al.* 2009), we speculated that the accumulation of IIB-SK1·2 would occur in the posterior region of migrating cells. To investigate this hypothesis, we performed a wound-healing assay using a MEF/3T3 Tet-Off cell-line expressing EGFP-IIB-SK1·2. Three hours after wounding, IIB-SK1·2 was widely distributed in cells located away from the wound edge, while it was highly accumulated at the posterior region of migrating cells adjacent to the wound (Fig. 5). Time-lapse imaging of MEF/3T3 Tet-Off cells coexpressing EGFP-IIB-SK1·2 and mCherry-IIB-WT demonstrated that when these cells ceased to migrate and then changed direction, IIB-SK1·2 located at the posterior region was released, and then reaccumulated at the new posterior region (Video S4, Fig. S2). These results indicate that IIB-SK1·2 accumulates at the posterior region when cells continue to migrate directionally.

IIB-SK1·2 displays a more restricted localization than IIA-SK1·2

To assess whether myosin IIA behaves similarly to myosin IIB, we generated the construct NMHC-IIA-SK1·2 (IIA-SK1·2), in which the region 1 and region 2 of NMHC-IIA (*MYH9*) (T1455-R1483 and L1544-E1570, respectively) were replaced with the corresponding portions of *MYH1*. The subcellular localization of IIA-SK1·2 in the migrating cell was examined. Wild-type (IIA-WT) and mutant (IIA-SK1·2) constructs were tagged with EGFP or mCherry, respectively, and were coexpressed in MEF/3T3 Tet-Off cells. EGFP-IIA-SK1·2 showed restricted localization to the central region, whereas mCherry-IIA-WT was distributed throughout the cell (Fig. 6A). This observed localization pattern was similar to that of EGFP-IIB-SK1·2 and mCherry-IIB-WT (Fig. 6B), suggesting that like IIB-SK1·2, IIA-SK1·2 is also unable to fold into the 10S form.

Myosin IIA is reportedly distributed throughout the cell, close to the cell periphery, whereas myosin IIB is favorably localized in the central region of HeLa cells (Maupin *et al.* 1994) and fibroblasts (Saitoh *et al.*

2001; Lo *et al.* 2004). In migrating cells, myosin IIA is localized to the newly formed lamella region prior to myosin IIB (Kolega 1998, 2003; Saitoh *et al.* 2001; Even-Ram *et al.* 2007; Sandquist and Means 2008; Vicente-Manzanares *et al.* 2008). When mCherry-IIA-SK1·2 was compared with EGFP-IIB-SK1·2, IIB-SK1·2 showed more restricted localization than IIA-SK1·2 (Fig. 6C). This tendency was also observed when mCherry-IIA-WT was compared with EGFP-IIB-WT (Fig. 6D), suggesting that the degree of restricted localization correlates with the specific properties of each NM-myosin II type, which is supported by the fact that myosin IIB has a higher assembling ability than myosin IIA (Murakami *et al.* 1995; Nakasawa *et al.* 2005).

IIB-SK1·2 functions properly in cytokinesis

To reveal the physiological significance of the 10S form of NM-myosin II, we examined whether IIB-SK1·2 is able to function properly in the cell. NMHC-IIB is a major isoform in COS-7 cells, and knockdown of NMHC-IIB induces cytokinesis defects, resulting in multinucleation, which is recoverable by re-expression of NMHC-IIB (Bao *et al.* 2005). We examined whether expression of IIB-SK1·2 can rescue multinucleation in NMHC-IIB-specific siRNA-treated COS-7 cells. Immunoblot analysis confirmed the reduction of endogenous NMHC-IIB, resulting from the specific siRNA treatment, and the expression of exogenous EGFP-NMHC-IIB (Fig. 7A). Seventy-two hours after transfection of COS-7 cells with the NMHC-IIB-specific siRNA, $50 \pm 5\%$ of cells expressing the EGFP-construct (i.e., without IIB-WT or IIB-SK1·2) were multinucleated (Fig. 7B,C). This multinucleation was rescued by expression of both EGFP-IIB-WT ($15 \pm 2\%$) and EGFP-IIB-SK1·2 ($18 \pm 4\%$). During cytokinesis, IIB-SK1·2 was localized at the cell equator in a similar manner to IIB-WT (Fig. 7D). These results demonstrate that IIB-SK1·2 can function properly in cytokinesis, indicating that IIB-SK1·2 can interact with actin filaments and that formation of a 10S form is not necessary for cytokinesis. However, during postmitotic spreading, EGFP-IIB-SK1·2 remained in the posterior of migrating daughter cells (Video S5, Fig. S3), supporting our finding that IIB-SK1·2 is not transported to the anterior region of migrating cells.

Expression of IIB-SK1·2 causes exclusion of endogenous myosin IIA from the posterior region of migrating cells

To elucidate the effect of IIB-SK1·2 expression on cell migration, wild-type and mutant EGFP-IIB constructs were expressed in a HeLa Tet-Off cell-line lacking endogenous NMHC-IIB; we studied the migratory behavior of these cells by tracing the location of the nucleus marked with mCherry-tagged nuclear

localization signal (NLS). Compared with control cells expressing EGFP, cells expressing IIB-WT showed a similar migration rate and directional persistence (Fig. 8A-C). Interestingly, cells expressing IIB-SK1·2 showed a higher migration rate and directional persistence than cells expressing IIB-WT.

Why the cells expressing IIB-SK1·2 migrate faster with keeping the direction than the cells expressing IIB-WT? We supposed that the organization of actin cytoskeleton is modulated by the expression of IIB-SK1·2, therefore, we attempted to observe the localization of endogenous myosin IIA in HeLa Tet-Off cells expressing EGFP-IIB constructs. In cells expressing IIB-WT, the localization of endogenous myosin IIA was not affected; however, in the cells expressing IIB-SK1·2, endogenous myosin IIA was excluded from the area where IIB-SK1·2 was localized (Fig. 8D, Fig. S4). We speculate that the segregation of the two NM-myosin II isoforms, specifically myosin IIA at the anterior region and myosin IIB at the posterior region, which occurred in the cells expressing IIB-SK1·2, results in this rigid migration pattern.

Discussion

In this study, we demonstrated that two portions of NMHC-IIB (*MYH10*), namely region 1 (S1462-R1490) and region 2 (L1551-E1577), are responsible for folding into the 10S form. The chimeric mutant, IIB-SK1·2, in which both regions were replaced with the corresponding regions of skeletal muscle myosin heavy chain (*MYH1*), did not fold into the 10S form under physiological conditions. This finding was confirmed by observing the recombinant full-length NM-myosin II molecules on electron micrographs directly. In addition, to reveal the role of the 10S form of NM-myosin II, we examined the behavior of IIB-SK1·2 in cells, and the effects of exogenous expression of IIB-SK1·2 on cellular motility. The results indicate that a folded conformation is necessary for maintaining inactivated NM-myosin II in the unassembled state, and for recruitment of NM-myosin II to another area of the cell.

Using single molecule negative stain electron microscopy with an image processing technique, Burgess *et al.* proposed a structural model of the 10S form of smooth muscle myosin (Burgess *et al.* 2007), in which the rod-like tail bends at two portions, and the resulting segments, 2 and 3, interact only with the one head (referred to as a “blocked head”) in an asymmetrical manner. According to this model, the second bend position is nearby E1535 of chicken smooth muscle myosin heavy chain. Notably, the corresponding residue of NMHC-IIB, E1529, is located between the region 1 and region 2 (Fig. S1). The region 2, positioned close to the second bend position within segment 3, almost overlaps the site identified to interact with the C-terminal lobe of RLC (Olney *et al.* 1996), and partially overlaps one of the sites identified to interact with the N-terminal lobe of RLC (Salzameda *et al.* 2006). The folded conformation is disrupted under high ionic concentrations *in vitro*, suggesting that electrostatic interaction is involved (Onishi and Wakabayashi, 1982; Trybus *et al.*, 1982). Recently, Jung *et al.* suggested that this electrostatic interaction occurs between the positively charged N-terminal region of RLC and the negatively charged tail region, and that phosphorylation of RLC could perturb these interactions (Jung *et al.* 2011). The negatively charged region of the tail is almost identical to the region 2 in this study (Fig. S1). According to the Burgess model (Burgess *et al.* 2007), the region 1, located close to the second bend position within segment 2, is likely to associate with ELC or the converter domain. ELC is important for the regulation of smooth muscle myosin activity (Kato *et al.* 2002) as well as RLC. The RLC-ELC interaction is stabilized by phosphorylation of RLC (Ni *et al.* 2012). We suppose that the RLC-ELC interaction interrupt the interaction between region 1 and ELC (or the converter domain) and leads the conformational change from a folded to an elongated form. Phosphorylation of RLC may disturb not only the association of the region 2 with RLC but also that of the region 1 with ELC (or converter domain). In this study, we have demonstrated that only the chimeric myosin IIB in which both region 1 and region 2

were replaced showed behaviors distinct from those of wild-type myosin IIB (Fig. 1), and this mutant was unable to fold into a 10S form (Fig. 2, Fig. 3). Chimeric NM-myosin II in which only the region 1 or only the region 2 was replaced showed behavior similar to that of wild-type myosin IIB (Fig. 1). We suppose that either the association of the region 1 with ELC (or converter domain) or that of the region 2 with RLC is sufficient for the formation of a folded conformation (probably incomplete 10S-form) to keep monomer in the inactivated state. For the formation of proper 10S form, we think both associations are necessary.

Under physiological conditions, phosphorylation of RLC at Ser19 induces an extended state that promotes assembly, whereas dephosphorylation induces a folded state that inhibits assembly (Craig et al. 1983; Ikebe et al. 1983; Trybus and Lowey 1984). Although dephosphorylated NM-myosin II and smooth muscle myosin are able to assemble, they require higher concentrations than their phosphorylated equivalents (Kendrick-Jones *et al.* 1987). Smooth muscle myosin depleted of its RLC is unable to fold into the 10S form, resulting in the formation of filaments under physiological conditions (Trybus and Lowey 1988). In this study, we demonstrated that the unfolded mutant, IIB-SK1·2, was also present as a filament. This filament form was indistinguishable from the reconstituted filament of purified platelet myosin (Niederman and Pollard 1975) under physiological conditions, even though their RLCs were unphosphorylated (Fig. 2G). The monomers observed by electron microscopy were in an extended conformation (Fig. 2H), indicating that if NM-myosin II forms an extended conformation, the monomer-filament equilibrium is shifted towards the filament state, even if the concentration of NM-myosin II is low. Moreover, these data indicate that phosphorylation of RLC is essential for the conformational change from a folded monomer to an extended monomer, but it is not necessary for filament assembly.

This study demonstrates that IIB-SK1·2 is able to function properly in cytokinesis (Fig. 7). Dynamic exchange of myosin II occurs during formation of the contractile ring in *Dictyostelium* cells (Yumura 2001), and myosin II filament assembly is regulated by phosphorylation of three Thr residues located in the C-terminal tail portion of its heavy chain. A myosin II mutant, in which these three Thr residues are replaced by Ala residues, is incorporated excessively into filaments and is able to rescue the growth of myosin II-null cells (Egelhoff et al. 1993). These properties are similar to those observed in this study for the myosin IIB-SK1·2 mutant. However, it is unclear why these mutants are able to perform cytokinesis properly. Although the monomer-filament equilibrium was shifted towards the filamentous state, this state is unlikely to be irreversible. We hypothesize that following dissociation of the IIB-SK1·2 monomer from the contractile ring, it is present in an extended conformation and can be quickly reformed into the contractile ring. This kind

of dynamic may be sufficient for NM-myosin II to function in cytokinesis. In other words, a folded monomer formation would not be necessary for NM-myosin II dynamics during cytokinesis.

Our results indicate that IIB-SK1·2 accumulated in the posterior region of migrating cells (Fig. 5, Video S4, Fig. S2). A similar result was also observed for the corresponding mutant of myosin IIA, IIA-SK1·2, although IIA-SK1·2 was not as restricted to the posterior region as IIB-SK1·2 (Fig. 6). A mutant of NMHC-IIA (Δ IQ2), which lacks the RLC-binding site in the neck domain, also accumulated in the posterior region during polarized migration (Breckenridge *et al.* 2009), and the authors predicted that this accumulation of Δ IQ2 is caused by stabilization of the filamentous form, probably by destabilizing the 10S form. Deletion mutants of NMHC-IIB that lack a part of the tail region, which include the region 1 and region 2 described in the current study, appeared in the Triton-insoluble fraction and accumulated abnormally in the posterior region of migrating cells (Rosenberg *et al.* 2008). It was hypothesized that the deletion mutants may be unable to fold into the 10S form. The results of the current study strongly support this hypothesis. Similar results were shown in *Dictyostelium* earlier (Yumura and Uyeda 1997). Taken together, the dynamic filament assembly-disassembly transition, which is regulated in a spatiotemporal manner, could be important for proper localization of NM-myosin II. If this dynamic is impaired, the filamentous NM-myosin II is accumulated in the posterior region of migrating cells, which shifts the monomer-filament equilibrium towards the filamentous state. We confirmed that the 10S form could contribute to recruitment of NM-myosin II to the anterior region of migrating cells, as previously suggested (Breckenridge *et al.* 2009).

We have demonstrated that IIB-SK1·2, but not IIB-WT, affects cellular migration rate and directional persistence (Fig. 8). Interestingly, IIB-SK1·2 also affected the subcellular localization of the endogenous myosin IIA, whereas IIB-WT did not. Endogenous myosin IIA was almost completely excluded from the region at which IIB-SK1·2 was localized (Fig. 8D, Fig. S4). This difference between the ability to affect endogenous myosin IIA localization is the most distinct behavior observed between IIB-SK1·2 and IIB-WT in this study. Myosin IIB has a greater assembling ability than myosin IIA (Murakami *et al.* 1995, Nakasawa *et al.* 2005); it was proposed that the isoform-specific distribution of myosin IIA and myosin IIB is related to the differences in their solubility, such that more soluble myosin IIA can redistribute into new protrusions in migrating cells (Sandquist and Means 2008). In the current study, IIA-WT was distributed more anteriorly than IIB-WT, and this difference was also observed for IIA-SK1·2 and IIB-SK1·2 (Fig. 6). Furthermore, myosin IIB has a higher duty ratio and a higher affinity for ADP than myosin IIA (Wang *et al.* 2003; Kovács *et al.* 2003); therefore, myosin IIB may maintain tension on actin filaments for longer periods of time with a lower expenditure of ATP than myosin IIA (Vicente-Manzanares *et al.* 2009). We hypothesize that

a highly assembled IIB-SK1·2 may occupy the actin filament and prevent interaction with myosin IIA, which may explain why myosin IIA was excluded from the region where IIB-SK1·2 was localized (Fig. 8). The resulting changes to the actomyosin structure and/or the force balance throughout the cell may lead to an alteration of migratory properties. It is noted that this phenomenon occurred only for cells expressing IIB-SK1·2, and not for cells expressing IIB-WT. Compared with IIB-WT, IIB-SK1·2 mutates the region 1 and region 2, which we propose as the sites responsible for folding to a 10S form. If our hypothesis is correct, it is plausible that, on occasion, IIB-WT folds into a 10S form in living cells. However, it is still unclear why IIB-SK1·2, but not IIB-WT, affects the rate and directional persistence of cell migration. In cell migration, NM-myosin II functions in the lamella of the anterior region as well as in the posterior region (Vicente-Manzanares *et al.* 2009). Myosin IIB creates a rear in migrating cells (Vicente-Manzanares *et al.* 2008). Myosin IIA is possibly the isoform that functions at the lamella, as predicted by its localization (Kolega 1998, 2003; Saitoh *et al.* 2001; Even-Ram *et al.* 2007; Sandquist and Means 2008; Vicente-Manzanares *et al.* 2008). Expression of IIB-SK1·2 resulted in almost complete exclusion of endogenous myosin IIA from the posterior region; thereby emphasizing the respective segregation of myosin IIA and myosin IIB isoforms to anterior and to posterior regions, respectively. We hypothesize that the complete segregation of the two NM-myosin II isoforms results in altered cellular migratory patterns.

The 10S form of smooth muscle myosin is present in airway smooth muscle cells (Milton *et al.* 2011). Although we could not show direct evidence of the presence of the 10S form of NM-myosin II in living cells, the results of the current study strongly indicate its presence. In conclusion, we demonstrated that the region 1 and region 2 of NMHC-IIB, and the corresponding portions of NMHC-IIA, are involved in the formation of the 10S form. Our results suggest that the role of the 10S form is to maintain NM-myosin II in the unassembled state to prevent the incorporation of inactive NM-myosin II into the cytoskeleton, and the folded monomers contribute to recruitment of NM-myosin II to the anterior region of migrating cells. Further investigation of the subcellular localization of a folded monomer and identification of putative 10S-interacting proteins might help to reveal specific roles of the 10S form.

Experimental procedures

Cell Culture

MRC-5 SV1 TG1 cells (SV40-transformant of human embryonic lung fibroblast MRC-5 cells) were obtained from RIKEN Cell Bank and were maintained in Minimum Essential Medium Eagle (MEM) alpha (GIBCO) supplemented with 10% fetal bovine serum (FBS) (BioSource), 50 U/ml penicillin, and 50 µg/ml streptomycin (GIBCO). MEF/3T3 Tet-Off cells and HeLa Tet-Off cells were obtained from Clontech and were maintained in Dulbecco's Modified Eagle Medium (DMEM) (GIBCO) supplemented with 10% FBS, 100 U/ml penicillin, and 100 µg/ml streptomycin. HeLa cells and COS-7 cells were obtained from Health Science Research Resources Bank and were maintained in DMEM supplemented with 10% FBS, 50 U/ml penicillin, and 50 µg/ml streptomycin. These cells were cultured at 37°C in humidified air containing 5% CO₂. Sf9 (*Spodoptera frugiperda*) cells were obtained from Invitrogen and were maintained in Sf900II serum-free medium (SFM) supplemented with 0.1% Pluronic F68 (GIBCO) under the condition of 27°C.

Antibodies and Reagents

The anti-NMHC-IIB polyclonal antibody targeting the carboxyl terminus of NMHC-IIB was used as described previously (Saitoh et al. 2001). The anti-NMHC-IIA polyclonal antibody targeting the carboxyl terminus of NMHC-IIA was used as described previously (Sato et al. 2007). Anti-GFP, rabbit polyclonal serum (A6455) was purchased from Molecular Probes. The anti- α -tubulin monoclonal antibody, coumarin-labeled phalloidin, and TRITC-labeled phalloidin were purchased from Sigma. The anti-RLCs polyclonal antibody, MLC-2 (FL-172), was purchased from Santa Cruz Biotechnology. Cy3-conjugated anti-rabbit IgG antibody was purchased from Jackson ImmunoResearch Laboratories. Horseradish peroxidase-labeled anti-rabbit IgG F(ab')₂ fragment was purchased from ICN Pharmaceuticals. Horseradish peroxidase-labeled anti-mouse IgG was purchased from Bio-Rad Laboratories. Fibronectin from human plasma was purchased from Roche Diagnostics. DAPI was purchased from Sigma.

Construction of Plasmid DNA

The plasmids pEGFP-NMHC-IIB and pTRE-EGFP-NMHC-IIA were a kind gift from Dr. Robert S. Adelstein of the National Institute of Health, US (Wei and Adelstein 2000). The pmCherry-N1 construct was a kind gift from Dr. Roger Y. Tsien of the University of California San Diego, US. The pmCherry-NLS construct was a kind gift from Dr. Toshiaki Imagawa of Hokkaido University, Japan. The pEGFP-C1 was purchased from Clontech, and the phmKikGR1-MCLinker was purchased from Medical & Biological Laboratories.

The pEGFP-NMHC-IIA was generated by replacing the TRE promoter of pTRE-EGFP-NMHC-IIA with the CMV promoter. The fragment obtained by restriction digestion of pEGFP-NMHC-IIB with AseI and HindIII was subcloned into the corresponding sites of pTRE-EGFP-NMHC-IIA. The pmCherry-NMHC-IIB and pmCherry-NMHC-IIA constructs were generated by replacing the sequence coding for the EGFP of pEGFP-NMHC-IIB and pEGFP-NMHC-IIA with that of mCherry. The PCR product coding mCherry

obtained by using the primer set described in Table S1, and pmCherry-N1 as a template was digested with AgeI and ScaI, and then mCherry was subcloned into the corresponding sites of pEGFP-NMHC-IIB and pEGFP-NMHC-IIA constructs to form pmCherry-NMHC-IIB and pmCherry-NMHC-IIA. The NMHC-IIB chimeric constructs, pEGFP-NMHC-IIB-SK1, pEGFP-NMHC-IIB-SK2, and pEGFP-NMHC-IIB-SK3, were generated by inverse PCR using the primer sets described in Table S1 and pEGFP-NMHC-IIB as a template. The plasmids were digested with XbaI and Sall, after verifying the nucleotide sequences between these sites, and the digestion products were subcloned into the same sites of pEGFP-NMHC-IIB-WT. The pEGFP-NMHC-IIB-SK1·2 and pEGFP-NMHC-IIB-SK1·3 were generated by subcloning the AclI/SacII digestion fragments of pEGFP-NMHC-IIB-SK2 and pEGFP-NMHC-IIB-SK3 into the corresponding sites of pEGFP-NMHC-IIB-SK1. The pmCherry-NMHC-IIB-SK1·2 was generated by subcloning the XbaI/Sall digestion fragment of pEGFP-NMHC-IIB-SK1·2 into the corresponding sites of pmCherry-NMHC-IIB. The NMHC-IIA chimeric constructs, pEGFP-NMHC-IIA-SK1·2 and pmCherry-NMHC-IIA-SK1·2, were generated using a two-step process as follows. Firstly, the pEGFP-NMHC-IIA-SK1 was generated by inverse PCR using the primer sets described in Table S1 and pEGFP-NMHC-IIA as a template. Then, pEGFP-NMHC-IIA-SK1·2 was generated by inverse PCR using the primer sets described in Table S1 and pEGFP-NMHC-IIA-SK1 as a template. The resulting plasmid was digested with EcoRI and SacII, after verifying the nucleotide sequences between these sites, and the digestion product was subcloned into the corresponding sites of pEGFP-NMHC-IIA-WT and pmCherry-NMHC-IIA-WT. The construction of pEGFP-NMHC-IIB-P1m will be described elsewhere. To generate pmCherry-NMHC-IIB-SK1·2-P1m, pEGFP-NMHC-IIB-P1m was digested with NheI and SacII, and the fragment containing the P1m portion was then subcloned into the corresponding sites of pmCherry-NMHC-IIB-SK1·2. To generate the phmKikGR-NMHC-IIB constructs, phmKikGR1-MCLinker was digested with KpnI, blunted using T4 DNA Polymerase (TaKaRa), and then digested using AseI. The fragment containing the hmKikGR1 coding region was subcloned into pEGFP-NMHC-IIB-WT and pEGFP-NMHC-IIB-SK1·2 at the AseI and ScaI sites, respectively. The nucleotide sequences of the DNA fragments amplified by PCR were verified by sequencing using DNA sequencer ABI PRISM 310 (Applied Biosystems).

Construction of Bacmid DNA

For baculovirus expression, the cDNAs coding for human nonmuscle type RLC (nmRLC; BAB62403) and HA-tagged human nonmuscle type ELC (nmELC; AAA59893) were amplified from the human brain cDNA library (Clontech) by PCR, using the primer sets described in Table S1. The PCR products were subcloned into the XhoI and KpnI, or EcoRI and HindIII sites of pFastBac Dual (Invitrogen) to generate the pFastBac-LCs. For the construction of the pFastBac-HTc-L21, the L21 sequence (Sano *et al.* 2002) was inserted into pFastBac-HTc (Invitrogen) using the QuikChange II XL Site-Directed Mutagenesis Kit (Stratagene) according to the manufacturer's protocol. The primer sets used are described in Table S1. To subclone the fragment coding NMHC-IIB-WT into pFastBac HTc-L21, a SacII site was inserted upstream of the NotI site of pENTR4 (Invitrogen). This insertion was achieved by digesting the PCR product obtained by

using the primer set described in Table S1 with KpnI and NotI, and then subcloning the digestion fragment into the corresponding sites of pENTR4. The pENTR4-NMHC-IIB-WT construct was generated by subcloning the EcoRI/SacII digestion fragment of pEGFP-NMHC-IIB-WT into the corresponding sites of pENTR4-Sac II. To generate the pFastBac-HTc-L21-NMHC-IIB-WT construct, pENTR4-NMHC-IIB-WT was digested with KpnI and NotI, blunted by incubation with T4 DNA polymerase, and then subcloned into the SalI and NotI sites of pFastBac-HTc-L21 blunted by incubation with T4 DNA polymerase. The pFastBac-HTc-L21-NMHC-IIB-SK1·2 was generated by subcloning the SbfI/NheI digested fragment of pEGFP-NMHC-IIB-SK1·2 into the corresponding sites of pFastBac-HTc-L21-NMHC-IIB-WT. The nucleotide sequences of the DNA fragments amplified by PCR were verified by sequencing using DNA sequencer ABI PRISM 310 (Applied Biosystems). Subsequently, bacmid DNAs were extracted from DH10Bac cells (Invitrogen) transformed with these pFastBac plasmids.

Transfection

Transfection of mammalian cells was performed using Lipofectamine 2000 (Invitrogen) according to the manufacturer's protocol. After incubation for 5 h under standard culturing conditions, cells were replated onto coverslips (Matsunami) or a glass based dish (IWAKI) precoated with 10 $\mu\text{g}/\text{ml}$ fibronectin for immunofluorescence or time-lapse imaging, respectively. Transfection of Sf9 cells to generate recombinant baculovirus was performed using polyethyleneimine (Sigma) according to a previously published protocol (Ogay *et al.* 2006). In brief, the purified bacmid DNA and polyethyleneimine were diluted into Sf900II SFM, respectively. These solutions were combined and incubated for 10 min, and then added to the cells. After incubation for 144 h, cells were centrifuged at $1,500 \times g$ for 5 min and the supernatant containing recombinant baculovirus was collected.

Protein Preparation

For purification of recombinant NM-myosin II, Sf9 cells in 250 ml medium (5×10^8 cells) were coinfecting with the baculoviruses encoding LCs and NMHC-IIB (WT or SK1·2). Sf9 cells were collected 72 h after infection and washed twice with phosphate-buffered saline (PBS). The cells were then extracted with five volumes of the extraction buffer (20 mM Tris-HCl, pH 7.5, 500 mM NaCl, 4 mM EDTA, 1% IGEPAL CA-630 (Sigma), 1 mM DTT, 5 $\mu\text{g}/\text{ml}$ pepstatin A, and $1 \times$ cOmplete EDTA-free protease inhibitor (Roche)), and then incubated for 30 min on ice. The extract was centrifuged at $100,000 \times g$ for 20 min at 4°C , after the addition of 5 mM MgCl_2 and 2 mM ATP. The supernatant was then subjected to ammonium sulfate fractionation. The fraction precipitating between 30% and 70% saturation was solubilized in buffer A (20 mM phosphate buffer, pH 7.4, 500 mM NaCl, 0.1 mM EGTA, and 0.1 mM PMSF) and then dialyzed against 50 volumes of buffer A with two changes. Following the addition of 3 μM F-actin and 1 mM DTT, the fraction was centrifuged at $100,000 \times g$ for 20 min at 4°C . The resulting pellet was washed with buffer B (20 mM MOPS, pH 7.5, 500 mM NaCl, 0.1 mM EGTA, and 1 mM DTT) and homogenized in buffer B containing 5 mM MgCl_2 and 5 mM ATP, using a Teflon-glass homogenizer. The solution was centrifuged at $100,000 \times g$

for 20 min at 4°C, and the resulting supernatant was then dialyzed against 100 volumes of low salt buffer (10 mM Imidazole-HCl, pH 7.0, 50 mM NaCl, 20 mM MgCl₂, and 1 mM DTT) with one change. The assembled NM-myosin II was precipitated by centrifugation at 22,000 × g for 15 min at 4°C, and then solubilized in high salt buffer (10 mM Imidazole-HCl, pH 7.0, 300 mM NaCl, and 1 mM DTT).

SDS-PAGE and Immunoblotting

SDS-polyacrylamide gel electrophoresis (SDS-PAGE) was performed using standard technique. For separation of phosphorylated RLC, Mn²⁺-Phos-tag SDS-PAGE was performed according to a previously described protocol (Hirata *et al.* 2009). The concentrations of Phos-tag acrylamide (NARD Institute) and MnCl₂ in the gel were 100 μM. Separated proteins were transferred to Immobilon-P membrane (Millipore). For RLC, the membrane was fixed with 0.25% glutaraldehyde in PBS for 45 min prior to blocking. The membrane was blocked with blocking buffer (5% skimmed milk and 0.05% Tween-20 in Tris-buffered saline (TBS)) for 60 min at 25°C. The membrane was incubated with primary antibody overnight at 4°C, followed by secondary antibody for 60 min at 25°C. The antibodies were diluted with blocking buffer as follows: anti-GFP rabbit polyclonal serum (1:10,000), anti-NMHC-IIB pAb (1:10,000), anti-NMHC-IIA pAb (1:10,000), anti-α-tubulin mAb (1:10,000), anti-RLC pAb (1:5,000), and secondary antibodies (1:10,000). The chemiluminescent signals were produced using Immobilon Western Chemiluminescent HRP Substrate (Millipore). The signals were detected using LAS-3000 (Fujifilm) and analyzed by using MultiGauge Version 2.2 software (Fujifilm).

Triton Solubility Assay

The Triton solubility assay was performed using the buffer described by Kolega (Kolega 1997) with some modifications. In brief, MRC-5 SV1 TG1 cells were transfected with pEGFP-NMHC-IIB constructs; after 48 h the cells were lysed with Triton X-100 lysis buffer (150 mM KCl, 20 mM PIPES, 10 mM Imidazole, pH 7.0, 0.05% Triton X-100, 1 mM MgCl₂, 1 mM EGTA, 1 mM DTT, 0.1 mM PMSF, 5 μg/ml aprotinin, 5 μg/ml leupeptin, 2 μg/ml pepstatin A, 1 mM Na₃VO₄, and 20 mM β-glycerophosphate) at 25°C. After 3 min, the lysates were centrifuged at 22,000 × g for 5 min at 4°C, and the supernatant was added to equal volumes of 2× Laemmli sample buffer. The insoluble fraction was collected by addition of 2× Laemmli sample buffer to cultured plate. Western blots were probed with anti-GFP rabbit polyclonal serum, and the signals were detected using LAS-3000 (Fujifilm) and analyzed using MultiGauge Version 2.2 software (Fujifilm).

Cell Lysate Preparation

HeLa cells were transfected with pEGFP-C1 or pEGFP-NMHC-IIB constructs and were lysed with ice-cold buffer D (50 mM Tris-HCl, pH7.4, 5 mM NaCl, 560 mM potassium acetate, 1 mM EDTA, 1 mM EGTA, 0.6% Triton X-100, 5 mM DTT, 1 mM PMSF, and 5 μg/ml leupeptin) 48 h after transfection. Following the addition of 5 mM MgCl₂ and 2 mM ATP, the lysates were centrifuged at 7800 × g for 15 min at 4°C to remove insoluble materials. The supernatant was split into halves; one half was diluted to 100 mM

potassium acetate with 4.6 volumes of ice-cold buffer D without potassium acetate or Triton X-100, and the other half was diluted to 400 mM potassium acetate with 4.6 volumes of ice-cold buffer D, including 365 mM potassium acetate without Triton X-100. The cell lysates were used for FCS measurements, as described below.

Electron Microscopy

Purified NM-myosin II (40 µg/ml) was incubated for 5 min at 4°C in a solution containing 150 mM or 400 mM NaCl, 4 mM MgCl₂, 2 mM ATP, 1 mM EGTA, 0.1 mM DTT, and 20 mM MOPS-NaOH (pH 7.5), and then diluted with three volumes of 80% glycerol and 100 mM or 400 mM NaCl. The samples were immediately sprayed onto mica, rotary-shadowed with platinum, and observed with a Hitachi H-7650 electron microscope operated at 80 kV with magnification 20,000× (Trybus and Lowey 1984; Katoh *et. al.* 1995).

Immunofluorescence

Transfected cells were fixed with 3.7% formaldehyde in PBS for 20 min, followed by permeabilization with 0.2% Triton X-100 in PBS for 5 min. The fixed cells were preincubated with 3% BSA in PBS for 30 min. Incubation with the anti-NMHC-IIB (1:1000) or the anti-NMHC-IIA (1:3000) polyclonal antibody was carried out for 60 min. Indirect immunolabeling was performed by incubation with Cy3-labeled anti-rabbit IgG antibody (1:500) containing coumarin-labeled phalloidin (0.5 µg/ml) or TRITC-labeled phalloidin (30 ng/mL) for 60 min. The images were captured using a conventional fluorescence microscope (BX50WI; Olympus) with a single chip color CCD camera (DP70; Olympus) and an objective lens (UPlanApo 20×/0.70 NA; Olympus or UPlanApo 60×/0.90 NA; Olympus) with DP Controller software (Olympus).

Knockdown - Rescue analysis

NMHC-IIB specific siRNA (GGAUCGCUACUAUUCAGGAUU) and nonsense siRNA (GCGCGCUUUGUAGGAUUCGUU) were purchased from Thermo Scientific Dharmacon. Knockdown-rescue analysis was performed as previously reported (Bao *et. al.*, 2005). In brief, COS-7 cells were transfected with 20 pmol NMHC-IIB specific siRNA or nonsense siRNA. After 24 h, the cells were transfected with pEGFP-C1 or pEGFP-NMHC-IIB constructs. After incubation for 5 h, cells were replated onto a coverslips coated with 10 µg/ml fibronectin and were grown for an additional 43 h. Multinucleated cells were counted after staining with DAPI (10 ng/ml).

Migration Analysis

The directional persistence of cell migration was obtained from time-lapse videos. Time-lapse images were captured by using an inverted microscope (IX71; Olympus) equipped with a single chip color CCD camera (DP70; Olympus) and an objective lens (LCPlanFl 20×/0.40 NA; Olympus); and cells were maintained in DMEM/F12 (1:1) (GIBCO) supplemented with 10% FBS, and warmed at 37°C on a

thermoplate (MATS-U55R30; Tokai Hit) during observation. The images were captured every 5 min and analyzed by using Lumina Vision version 2.4.2 software (Mitani Corporation). To trace the migration path, HeLa Tet-Off cells were cotransfected with pmCherry-NLS and pEGFP constructs. Migration paths were determined by the centroid of mCherry-NLS obtained from each frame using ImageJ software and MTrackJ plugin. The directional persistence (D/T ratio) was calculated as a ratio of the direct distance during a 3 h period (D) and the total migration length (T).

FCS

FCS measurements (Rigler et al., 1993; Kitamura et al., 2006) were performed using a ConfoCor 2 system and C-Apochromat 40×/1.2NA UV-VIS-IR Korr water immersion objective (Carl Zeiss). EGFP was excited at 488 nm. Confocal pinhole diameters were adjusted to 70 μm at 488 nm. Emission signals were detected with a 505 nm long-pass filter for EGFP. Supernatant fluorescence signals were recorded using Lab-Tek 8-well chamber slides (NUNC, Rochester, NY) at 25°C. The fluorescence autocorrelation functions, $G(\tau)$, from which the average correlation time (τ) and the absolute number of fluorescent proteins in the detection volume were calculated, were obtained using Equation 1 below, where $I(t+\tau)$ is the fluorescence intensity obtained by the single photon counting method in a detection volume at a delay time τ (brackets denote ensemble averages):

$$G(\tau) = \frac{\langle I(t) \cdot I(t + \tau) \rangle}{\langle I(t) \rangle^2} \quad (1)$$

Curve fitting for the multi-component model is given by Equation 2 below, where: F_i and τ_i are the fraction and diffusion time of component i , respectively; N is the average number of fluorescent molecules in the detection volume defined by the beam waist w_0 and the axial radius z_0 ; s is the structure parameter representing the ratio of w_0 and z_0 ; P_t is the triplet fraction; and τ_t is the relaxation time of the triplet state:

$$G(\tau) = 1 + \frac{1}{N} \left[\sum_i F_i \left(1 + \frac{\tau}{\tau_i}\right)^{-1} \left(1 + \frac{\tau}{s^2 \tau_i}\right)^{-\frac{1}{2}} + \frac{P_t}{1 - P_t} \exp\left(-\frac{\tau}{\tau_t}\right) \right] \quad (2)$$

$G(\tau)$ s in aqueous solutions were measured for 45 s. Following pinhole adjustment, diffusion time and structure parameter were determined using a 10^{-7} M rhodamine6G (Rh6G) solution as a standard before measurements. A single-component fitting model ($i=1$) was performed in all analyses.

FRAP

MRC-5 SV1 TG1 cells were cotransfected with pEGFP-NMHC-IIB-SK1.2 and pmCherry-NMHC-IIB-WT and replated onto a glass base dish coated with 10 μg/ml fibronectin. Cells were observed using a LSM 510 META microscope (Carl Zeiss) equipped with a C-Apochromat 40×/1.2NA UV-VIS-IR DIC water immersion objective (Carl Zeiss) and a heated stage (37 °C) and under circulation of

5% CO₂-95% air. EGFP and mCherry were excited at 488 nm and 543 nm, respectively. Fluorescence signals were split by using HFT488/543 from excitation beams. Green and red fluorescence signals were separated by using a dichroic mirror (NFT570) and were obtained through a band-pass filter (BP505-530) and a spectral separation (616-798 nm), respectively. Pinhole diameters were settled as 145 μm (2.08 Airy Unit) as a green channel and 191 μm (1.99 Airy Unit) as a red channel. Regions of interest (ROIs) were photobleached for 5.5 s by irradiation with a 488 nm diode laser at 100% power and a 543 nm He-Ne laser at 100% power. Fluorescent images after photobleaching in living cells were captured in every 10 s. Relative fluorescence intensity (RFI) was calculated equation 3 below, where $I_{ROI}(t)$ is a time-series of fluorescence intensity in a photobleached ROI, $I_{Ref}(t)$ is a time-series of fluorescence intensity in a non-photobleached ROI as a reference and $I_{ROI}(0)$ and $I_{Ref}(0)$ are fluorescence intensity before photobleaching in the photobleached ROI and non-photobleached ROI. Background signals were subtracted from all fluorescence intensities before calculation.

$$RFI = [I_{ROI}(t) \cdot I_{Ref}(0)] / [I_{Ref}(t) \cdot I_{ROI}(0)] \quad (3)$$

RFI curves were fitted by using a single-component exponential association model in equation (4) below, where A is a maximum recovery, k is a dissociation rate, and c is a baseline.

$$I(t) = A[1 - \exp(-kt)] + c \quad (4)$$

Half recovery times were obtained as the reciprocals of the dissociation rates were multiplied by $\ln(2) = 0.693$.

Photoconversion Experiment

MRC-5 SV1 TG1 cells were transfected with phmKikGR-NMHC-IIB-SK1.2 or phmKikGR-NMHC-IIB-WT, and replated onto a glass base dish coated with 10 μg/ml fibronectin. Time-lapse images were captured using an inverted microscope (Ti-E; Nikon) and confocal laser microscope system (A1R; Nikon) equipped with an oil immersion objective lens (Plan Apo - VC 60×/1.40 NA; Nikon). Cells were maintained in DMEM/F12 (1:1) (GIBCO) supplemented with 10% FBS and were warmed in a 37°C chamber (INUBG2H-TIZB; Tokai Hit) during observation. Images were captured every 3 min and were analyzed by using NIS-Elements C software (Nikon). Photoconversion was performed by a diode laser (405 nm), and unphotoconverted mKikGR and photoconverted mKikGR were excited using an Ar (488 nm) and a DPSS (561 nm) laser, respectively.

Acknowledgments

We are grateful to the Nikon Imaging Center at Hokkaido University for being very helpful with confocal microscopy, image acquisition, and analysis. We are grateful to Dr. Robert S Adelstein for helpful advice on knockdown-rescue analysis. We are also grateful to Dr. Michio Yazawa for his helpful discussion and critical reading of the manuscript. We thank Ms. Akiko Fujita, and Ms. Mariko Mitsuhashi for assistance with the construction of plasmids.

This work was supported by Grants-in-Aid for Scientific Research (C) 22570129 from the Japan Society for the Promotion of Science. This work was also supported by the Global COE Program (Project No. B01: Catalysis as the Basis for Innovation in Materials Science) from the Ministry of Education, Culture, Sports, Science and Technology, Japan.

References

- Bao, J., Jana, S.S. & Adelstein, R.S. (2005) Vertebrate nonmuscle myosin II isoforms rescue small interfering RNA-induced defects in COS-7 cell cytokinesis. *J. Biol. Chem.* **280**, 19594–19599.
- Berg, J.S., Powell, B.C. & Cheney, R.E. (2001) A millennial myosin census. *Mol. Biol. Cell* **12**, 780-794.
- Breckenridge, M.T., Dulyaninova, N.G. & Egelhoff, T.T. (2009) Multiple regulatory steps control mammalian nonmuscle myosin II assembly in live cells. *Mol. Biol. Cell* **20**, 338-347.
- Burgess, S.A., Yu, S., Walker, M.L., Hawkins, R.J., Chalovich, J.M. & Knight, P.J. (2007) Structures of smooth muscle myosin and heavy meromyosin in the folded, shutdown state. *J. Mol. Biol.* **372**, 1165-1178.
- Conti, M.A., Even-Ram, S., Liu, C., Yamada, K.M. & Adelstein, R.S. (2004) Defects in cell adhesion and the visceral endoderm following ablation of nonmuscle myosin heavy chain II-A in mice. *J. Biol. Chem.* **279**, 41263-41266.
- Conti, M.A. & Adelstein, R.S. (2008) Nonmuscle myosin II moves in new directions. *J. Cell Sci.* **121**, 11-18.
- Craig, R., Smith, R. & Kendrick-Jones, J. (1983) Light-chain phosphorylation controls the conformation of vertebrate non-muscle and smooth muscle myosin molecules. *Nature* **302**, 436-439.
- Cross, R.A., Cross, K.E. & Sobieszek, A. (1986) ATP-linked monomer-polymer equilibrium of smooth muscle myosin: the free folded monomer traps ADP.Pi. *EMBO J.* **5**, 2637-2641.
- Egelhoff, T.T., Lee, R.J. & Spudich, J.A. (1993) Dictyostelium myosin heavy chain phosphorylation sites regulate myosin filament assembly and localization in vivo. *Cell* **75**, 363-371.
- Even-Ram, S., Doyle, A.D., Conti, M.A., Matsumoto, K., Adelstein, R.S. & Yamada, K.M. (2007) Myosin IIA regulates cell motility and actomyosin–microtubule crosstalk. *Nat. Cell Biol.* **9**, 299-309.
- Golomb, E., Ma, X., Jana, S.S., Preston, Y.A., Kawamoto, S., Shoham, N.G., Goldin, E., Conti, M.A., Sellers, J.R. & Adelstein, R.S. (2004) Identification and characterization of nonmuscle myosin II-C, a new member of the myosin II family. *J. Biol. Chem.* **279**, 2800-2808.
- Habuchi, S., Tsutsui, H., Kochaniak, A.B., Miyawaki, A. & van Oijen, A.M. (2008) mKikGR, a monomeric photoswitchable fluorescent protein. *PLoS One* **3**, e3944.

- Hirata, N., Takahashi, M. and Yazawa, M. (2009) Diphosphorylation of regulatory light chain of myosin IIA is responsible for proper cell spreading. *Biochem. Biophys. Res. Commun.* **381**, 682-687.
- Horowitz, A., Trybus, K.M., Bowman, D.S. & Fay, F.S. (1994) Antibodies probe for folded monomeric myosin in relaxed and contracted smooth muscle. *J. Cell Biol.* **126**, 1195-1200.
- Ikebe, M., Hinkins, S. & Hartshorne, D.J. (1983) Correlation of enzymatic properties and conformation of smooth muscle myosin. *Biochemistry* **22**, 4580-4587.
- Ikebe, M., Ikebe, R., Kamisoyama, H., Reardon, S., Schwonek, J.P., Sanders, C.R. & Matsuura, M. (1994) Function of the NH₂-terminal domain of the regulatory light chain on the regulation of smooth muscle myosin. *J. Biol. Chem.* **269**, 28173-28180.
- Ikebe, M. (2008) Regulation of the function of mammalian myosin and its conformational change. *Biochem. Biophys. Res. Commun.* **369**, 157-164.
- Jung, H.S., Komatsu, S., Ikebe, M. and Craig, R. (2008) Head-head and head-tail interaction: a general mechanism for switching off myosin II activity in cells. *Mol. Biol. Cell.* **19**, 3234-3242.
- Jung, H.S., Billington, N., Thirumurugan, K., Salzameda, B., Cremo, C.R., Chalovich, J.M., Chantler, P.D. & Knight, P. (2011) Role of the tail in the regulated state of myosin 2. *J. Mol. Biol.* **408**, 863-878.
- Katoh, T., Kodama, T., Fukushima, A., Yazawa, M. and Morita, F. (1995) Evidence for involvement of a 12-residue peptide segment of the heavy chain in the neck region of smooth muscle myosin in formation of the 10S conformation. *J. Biochem.* **118**, 428-434.
- Katoh, T., Konishi, K. and Yazawa, M. (2002) Essential light chain modulates phosphorylation-dependent regulation of smooth muscle myosin. *J. Biochem.* **131**, 641-645.
- Kendrick-Jones, J., Smith, R.C., Craig, R. & Citi, S. (1987) Polymerization of vertebrate non-muscle and smooth muscle myosins. *J. Mol. Biol.* **198**, 241-252.
- Kitamura, A., Kubota, H., Pack, C-Gi., Matsumoto, G., Hirayama, S., Takahashi, Y., Kimura, H., Kinjo, M., Morimoto, R.I. & Nagata, K. (2006) Cytosolic chaperonin prevents polyglutamine toxicity with altering the aggregation state. *Nat. Cell Biol.* **8**, 1163-1169.
- Kolega, J. (1997) Asymmetry in the distribution of free versus cytoskeletal myosin II in locomoting

microcapillary endothelial cells. *Exp. Cell Res.* **231**, 66-82.

Kolega, J. (1998) Cytoplasmic dynamics of myosin IIA and IIB: spatial 'sorting' of isoforms in locomoting cells. *J. Cell Sci.* **111**, 2085–2095.

Kolega, J. (2003) Asymmetric distribution of myosin IIB in migrating endothelial cells is regulated by a rho-dependent kinase and contributes to tail retraction. *Mol. Biol. Cell* **14**, 4745-4757.

Kovács, M., Wang, F., Hu, A., Zhang, Y. & Sellers, J.R. (2003) Functional divergence of human cytoplasmic myosin II: kinetic characterization of the non-muscle IIA isoform. *J. Biol. Chem.* **278**, 38132-38140.

Lo, C.-M., Buxton, D.B., Chua, G.C. H., Dembo, M., Adelstein, R.S. & Wang, Y.-L. (2004) Nonmuscle myosin IIB is involved in the guidance of fibroblast migration. *Mol. Biol. Cell* **15**, 982-989.

Lowey, S. & Trybus, K.M. (2010) Common structural motifs for the regulation of divergent class II myosins. *J. Biol. Chem.* **285**, 16403-16407.

Matsumura, F. (2005) Regulation of myosin II during cytokinesis in higher eukaryotes. *Trends Cell Biol.* **15**, 371-377.

Maupin, P., Phillips, C.L., Adelstein, R.S. & Pollard, T. D. (1994) Differential localization of myosin-II isozymes in human cultured cells and blood cells. *J. Cell Sci.* **107**, 3077-3090.

Milton, D.L., Schneck, A.N., Ziech, D.A., Ba, M., Facemyer, K.C., Halayko, A.J., Baker, J.E., Gerthoffer, W.T. & Cremo, C.R. (2011) Direct evidence for functional smooth muscle myosin II in the 10S self-inhibited monomeric conformation in airway smooth muscle cells. *Proc. Natl. Acad. Sci. USA* **108**, 1421-1426.

Murakami, N., Singh, S.S., Chauhan, V.P. & Elzinga, M. (1995) Phospholipid binding, phosphorylation by protein kinase C, and filament assembly of the COOH terminal heavy chain fragments of nonmuscle myosin II isoforms MIIA and MIIB. *Biochemistry* **34**, 16046-16055.

Nakasawa, T., Takahashi, M., Matsuzawa, F., Aikawa, S., Togashi, Y., Saitoh, T., Yamagishi, A. & Yazawa, M. (2005) Critical regions for assembly of vertebrate nonmuscle myosin II. *Biochemistry* **44**, 174-183.

Ni, S., Hong, F., Haldeman, B.D., Baker, J.E., Facemyer, K.C. & Cremo, C.R. (2012). Modification of interface between regulatory and essential light chains hampers phosphorylation-dependent activation of smooth muscle myosin. *J. Biol. Chem.* **287**, 22068-22079.

- Niederman, R. & Pollard, T.D. (1975) Human platelet myosin. II. in vitro assembly and structure of myosin filaments. *J. Cell Biol.* **67**, 72-92.
- Ogay, I.D., Lihoradova, O.A., Azimova, Sh.S., Abdulkarimov, A.A., Slack, J.M. & Lynn, D.E. (2006) Transfection of insect cell lines using polyethylenimine. *Cytotechnology* **51**, 89-98.
- Olney, J.J., Sellers, J.R. & Cremona, C.R. (1996) Structure and function of the 10 S conformation of smooth muscle myosin. *J. Biol. Chem.* **271**, 20375-20384.
- Onishi, H. & Wakabayashi, T. (1982) Electron microscopic studies of myosin molecules from chicken gizzard muscle I: the formation of the intramolecular loop in the myosin tail. *J. Biochem.* **92**, 871-879.
- Rigler, R., Mets, Ü., Widengren, J. & Kask, P. (1993) Fluorescence correlation spectroscopy with high count rate and low background: analysis of translational diffusion. *Eur. Biophys. J.* **22**, 169-175.
- Rosenberg, M., Straussman, R., Ben-Ya'acov, A., Ronen, D. & Ravid, S. (2008) MHC-IIB filament assembly and cellular localization are governed by the rod net charge. *PLoS ONE* **3**, e1496.
- Saitoh, T., Takemura, S., Ueda, K., Hosoya, H., Nagayama, M., Haga, H., Kawabata, K., Yamagishi, A. & Takahashi, M. (2001) Differential localization of non-muscle myosin II isoforms and phosphorylated regulatory light chain in human MRC-5 fibroblasts. *FEBS Lett.* **509**, 365-369.
- Salzameda, B., Facemyer, K.C., Beck, B.W. & Cremona, C.R. (2006) The N-terminal lobes of both regulatory light chains interact with the tail domain in the 10 S-inhibited conformation of smooth muscle myosin. *J. Biol. Chem.* **281**, 38801-38811.
- Sandquist, J.C. & Means, A.R. (2008) The C-terminal tail region of nonmuscle myosin II directs isoform-specific distribution in migrating cells. *Mol. Biol. Cell* **19**, 5156-5167.
- Sano, K., Maeda, K., Oki, M. & Maeda, Y. (2002) Enhancement of protein expression in insect cells by a lobster tropomyosin cDNA leader sequence. *FEBS Lett.* **532**, 143-146.
- Sato, M.K., Takahashi, M. & Yazawa, M. (2007) Two regions of the tail are necessary for the isoform-specific functions of nonmuscle myosin IIB. *Mol. Biol. Cell* **18**, 1009-1017.

- Sellers, J.R. & Knight, P.J. (2007) Folding and regulation in myosins II and V. *J. Muscle Res. Cell Motil.* **28**, 363-370.
- Somlyo, A.V., Butler, T.M., Bond, M. & Somlyo, A.P. (1981) Myosin filaments have non-phosphorylated light chains in relaxed smooth muscle. *Nature* **294**, 567-569.
- Trybus, K.M., Huiatt, W.T. & Lowey, S. (1982) A bent monomeric conformation of myosin from smooth muscle. *Proc. Natl. Acad. Sci. USA* **79**, 6151-6155.
- Trybus, K.M. & Lowey, S. (1984) Conformational states of smooth muscle myosin. Effects of light chain phosphorylation and ionic strength. *J. Biol. Chem.* **259**, 8564-8571.
- Trybus, K.M. & Lowey, S. (1988) The regulatory light chain is required for folding of smooth muscle myosin. *J. Biol. Chem.* **263**, 16485-16492.
- Tullio, A.N., Accili, D., Ferrans, V.J., Yu, Z.X., Takeda, K., Grinberg, A., Westphal, H., Preston, Y.A. & Adelstein, R.S. (1997) Nonmuscle myosin II-B is required for normal development of the mouse heart. *Proc. Natl. Acad. Sci. USA* **94**, 12407-12412.
- Vicente-Manzanares, M., Koach, M.A., Whitmore, L., Lamers, M.L. & Horwitz, A.F. (2008) Segregation and activation of myosin IIB creates a rear in migrating cells. *J. Cell Biol.* **183**, 543-554.
- Vicente-Manzanares, M., Ma, X., Adelstein, R.S. & Horwitz, A.R. (2009) Non-muscle myosin II takes centre stage in cell adhesion and migration. *Nat. Rev. Mol. Cell Biol.* **10**, 778-790.
- Wang, F., Kovács, M., Hu, A., Limouze, J., Harvey, E.V. & Sellers, J.R. (2003) Kinetic mechanism of non-muscle myosin IIB: functional adaptations for tension generation and maintenance. *J. Biol. Chem.* **278**, 27439-27448.
- Wang, A., Ma, X., Conti, M.A., Liu, C., Kawamoto, S. & Adelstein, R.S. (2010) Nonmuscle myosin II isoform and domain specificity during early mouse development. *Proc. Natl. Acad. Sci. USA* **107**, 14645-14650.
- Wei, Q. & Adelstein, R.S. (2000) Conditional expression of a truncated fragment of nonmuscle myosin II-A alters cell shape but not cytokinesis in HeLa cells. *Mol. Biol. Cell* **11**, 3617-3627.
- Yumura, S. (2001) Myosin II dynamics and cortical flow during contractile ring formation in Dictyostelium

cells. *J. Cell Biol.* **154**, 137-146.

Yumura, S. & Uyeda, TQ. (1997) Myosin II can be localized to the cleavage furrow and to the posterior region of *Dictyostelium amoebae* without control by phosphorylation of myosin heavy and light chains. *Cell Motile. Cytoskeleton.* **36**, 313-22.

Figure Legends

Figure 1. Chimeric myosin IIB-SK1·2 behaves differently to wild-type myosin IIB. (A) NMHC-IIB constructs used to identify the tail portions responsible for folding into the 10S form. The regions 1 (S1462-R1490), 2 (L1551-E1577), and 3 (E1588-A1617) are indicated by green, red, and blue boxes, respectively. (B) Immunoblot of Triton soluble (S) and insoluble (I) fractions of MRC-5 SV1 TG1 cells expressing the indicated EGFP-IIB constructs, probed with an anti-GFP antibody. (C) The percentage of each EGFP-IIB extracted in the Triton X-100 soluble fractions. Data represent the mean \pm SD from four independent experiments. *** $p < 0.0005$. (D) Images of MRC-5 SV1 TG1 cells coexpressing EGFP-IIB constructs (IIB-WT, IIB-SK1, IIB-SK2, IIB-SK3, IIB-SK1·2, and IIB-SK1·3) and mCherry-IIB-WT. Cells were fixed 18 h after plating onto coverslips, and images were captured using a conventional fluorescence microscope (BX50WI) and an objective lens (UPlanApo 60 \times /0.90 NA). The first and second columns display images of each EGFP-IIB construct and mCherry-IIB-WT, respectively. The third column displays a merged image of EGFP-IIBs and mCherry-IIB-WT. The fourth column displays an image of F-actin stained by coumarin-phalloidin. Bar, 5 μ m. (E) The histogram of the ratios of the localized area size of the EGFP-IIB-SK1·2 (gray bars) or EGFP-IIB-WT (black bars) to that of mCherry-IIB-WT. The localized area sizes of each fluorescent protein in the cells were measured using ImageJ software, and the ratios of that of EGFP-IIBs to that of mCherry-IIB-WT at each cell were calculated. $n=20$ (EGFP-IIB-WT) and 54 (EGFP-IIB-SK1·2).

Figure 2. Electron micrographs of recombinant myosin IIB molecules. (A) Coomassie brilliant blue-stained SDS-PAGE gel showing the purified recombinant NM-myosin IIs. Arrowheads indicate heavy chain (top), RLC (middle), and ELC (bottom). The arrow indicates the remaining actin that was used for purification. (B) Immunoblot analysis to investigate the phosphorylation levels of RLC. Purified wild-type (IIB-WT) and mutant (IIB-SK1·2) NM-myosin IIs were subjected to Mn^{2+} -Phos-tag SDS-PAGE, followed by immunoblotting and detection with an anti-RLC antibody. Whole cell extract (WCE) of MRC5 SV1 TG1 cells was used as a control. Diphosphorylated RLC at Ser19 and Thr18 (2P), monophosphorylated RLC at Ser19 (1P), and dephosphorylated RLC (0P) are indicated. (C-H) Representative rotary-shadowed images of purified recombinant myosin IIB-WT (C - E) and IIB-SK1·2 (F - H), in 400 mM (C and F) or 110 mM (D, E, G, and H) NaCl with 2 mM ATP and 4 mM $MgCl_2$. Bar, 100 nm. (E) Enlarged images of 10S form of IIB-WT. Bar, 50 nm. (I) The percentage of NM-myosin II molecules in the filamentous (black bars), extended (gray bars), and folded (10S) (light gray bars) states. At least 250 molecules were counted from 30 independent fields per sample.

Figure 3. FCS analysis of HeLa cell lysates expressing EGFP-IIB constructs. (A) The autocorrelation functions obtained from FCS measurement were normalized at the value of $G(0)$. Solid lines indicate the data under low salt conditions (100 mM potassium acetate, 2 mM ATP, and 5 mM $MgCl_2$). Dotted lines indicate the data under high salt conditions (400 mM potassium acetate, 2mM ATP, and 5mM $MgCl_2$). (B) Diffusion times

obtained by fitting the autocorrelation functions with a single-component model. White and black bars indicate the results obtained under low and high salt conditions, respectively. Data represent mean \pm SD of three independent experiments. (C) Normalized diffusion times of each EGFP-IIB to those of EGFP at each salt condition. White and black bars indicate the results obtained under low and high salt conditions, respectively. Data represent mean \pm SD of three independent experiments. * $p < 0.05$.

Figure 4. Dynamic properties of IIB-SK1·2 in the cell. (A-C) FRAP analysis of MRC-5 SV1 TG1 cells coexpressing EGFP-IIB-SK1·2 (green) and mCherry-IIB-WT (red). The area in the almost center between the nucleus and the plasma membrane of the cell was photobleached. We analyzed the nonmigrating cells in which stress fibers were developed throughout the cells. (A) Still images captured from Video S1. The circle area indicated by the white arrow was photobleached. Bar, 5 μm . (B) The time course of fluorescence recovery after photobleaching of mCherry-IIB-WT and EGFP-IIB-SK1·2. The result showing the smoothest behavior on the recovery process (open circles in Fig. 4C) was chosen as a representative. (C) Dot plots showing the half-recovery times from 11 cells. Data from each of the 11 individual cells are indicated with different symbols. (D) Photoconversion analysis of MRC-5 SV1 TG1 cells expressing mKikGR-IIB-WT or mKikGR-IIB-SK1·2. Still images captured from Video S2 and S3. The two upper-most panels display whole-cell images before photoconversion. Bar, 5 μm . The twelve lower-most panels display enlarged images of the white rectangular regions in the upper panels. Red areas indicate the photoconversion molecules. Bar, 2 μm . (E-F) Time course of the changes in major axis length (E) and total fluorescence intensity (F) of the area on the fiber structure, where showing red fluorescence of photoconverted mKikGR-IIB-WT (closed triangles) or mKikGR-IIB-SK1·2 (closed circles). The still images captured from Video S2 and S3 were analyzed by ImageJ software. (G) Images of MRC-5 SV1 TG1 cells coexpressing EGFP-IIB-P1m (first panel) and mCherry-IIB-SK1·2-P1m (second panel). The third panel is a merged image of EGFP-IIB-P1m and mCherry-IIB-SK1·2-P1m. The fourth panel is an image of F-actin stained by coumarin-phalloidin. Images were captured using a conventional fluorescence microscope (BX50WI) and an objective lens (UPlanApo 60 \times /0.90 NA). Bar, 5 μm .

Figure 5. Localization of EGFP-IIB-SK1·2 in cells during wound healing. MEF/3T3 Tet-Off cells expressing EGFP-IIB-SK1·2 were grown until confluent. Cells were fixed 3 h after wounding and stained for F-actin with TRITC-phalloidin. Images were captured using a conventional fluorescence microscope (BX50WI) and an objective lens (UPlanApo 20 \times /0.70 NA). Upper and lower panels display images of cells located away from and adjacent to the wound edge, respectively. Bar, 20 μm .

Figure 6. Localization of IIA-WT, IIA-SK1·2, IIB-WT, and IIB-SK1·2 in the cell. MEF/3T3 cells coexpressing the indicated constructs were fixed and then stained by coumarin-phalloidin. (A) EGFP-IIA-SK1·2 and mCherry-IIA-WT. (B) EGFP-IIB-SK1·2 and mCherry-IIB-WT. (C) EGFP-IIB-SK1·2 and mCherry-IIA-SK1·2. (D) EGFP-IIB-WT and mCherry-IIA-WT. The first and second columns display

images of the EGFP-fused construct and mCherry-fused construct, respectively. The third column displays merged images of EGFP and mCherry. The fourth column displays images of F-actin stained by coumarin-phalloidin. Images were captured using a conventional fluorescence microscope (BX50WI) and an objective lens (UPlanApo 60×/0.90 NA). Bar, 5 μ m.

Figure 7. Rescue of cytokinesis defects in NMHC-IIB siRNA-treated COS-7 cells following expression of EGFP-IIB constructs. Twenty-four hours after transfection with NMHC-IIB siRNA or nonsense siRNA, COS-7 cells were transfected with pEGFP, pEGFP-IIB-WT, or pEGFP-IIB-SK1·2. The culture was maintained for a further 48 h. (A) Immunoblot analysis of expression levels of endogenous NMHC-IIB and exogenous EGFP-NMHC-IIBs probed with an anti-NMHC-IIB antibody. The slow migrating bands in the upper panel are EGFP-NMHC-IIB-WT and IIB-SK1·2. An anti- α -tubulin antibody was used as a loading control. (B) Cells were fixed and stained with an anti-NMHC-IIB antibody (red) and DAPI (blue). Images were captured using a conventional fluorescence microscope (BX50WI) and an objective lens (UPlanApo 20×/0.70 NA). Green color in the lower panels indicates the exogenously expressed EGFP-IIB constructs. Note that the cells lacking endogenous NMHC-IIB were multinucleated (upper right panel), and that the multinucleation was rescued by the expression of EGFP-IIB-SK1·2 as well as EGFP-IIB-WT. Bar, 20 μ m. (C) The percentage of multinucleated cells, as determined by counting at least 100 GFP-positive cells per experiment. Data represent mean \pm SD of three independent experiments. ****p<0.005.** (D) Images of EGFP-IIB-WT or EGFP-IIB-SK1·2 during cytokinesis of COS-7 cells treated with NMHC-IIB-specific siRNA. Images were captured using a conventional fluorescence microscope (BX50WI) and an objective lens (UPlanApo 60×/0.90 NA). Bar, 5 μ m.

Figure 8. Effects of exogenous expression of IIB-SK1·2 on cellular migration. (A) Analyses of migration paths of HeLa Tet-Off cells expressing EGFP (left), EGFP-IIB-WT (middle), or EGFP-IIB-SK1·2 (right) with the mCherry-NLS construct. The paths of eight representative cells are shown by different symbols and colors. (B) Cellular migration rates, calculated as the total migration length divided by the total time. Data represent mean \pm SD, n = 24. *****p<0.0005.** (C) Directional persistence, calculated as the ratio of the distance during a 3 h period and the total migration length. Data represent mean \pm SD, n = 24. *****p<0.0005.** (D) Localization of endogenous myosin IIA in HeLa Tet-Off cells expressing EGFP (top panels), EGFP-IIB-WT (middle panels), or EGFP-IIB-SK1·2 (bottom panels). The second column displays images of endogenous myosin IIA immunostaining. The third column displays merged images of EGFP, EGFP-IIB-WT, or EGFP-IIB-SK1·2, and endogenous myosin IIA. The fourth column displays images of F-actin stained by coumarin-phalloidin. Images were captured using a conventional fluorescence microscope (BX50WI) and an objective lens (UPlanApo 60×/0.90 NA). Bar, 5 μ m. Additional representative images of cells expressing EGFP-IIB-WT or EGFP-IIB-SK1·2 are displayed in Supplemental Fig. S4.

Supporting information/Supplemental material

The following Supporting Information can be found in the online version of the article:

Figure S1 Sequence alignment of human class II myosin heavy chains in regions corresponding to *MYH10* (amino acids 1401–1700).

Figure S2 Still images from Video S4 focused on the direction change of migrating MEF/3T3 Tet-Off cells coexpressing EGFP-IIB-SK1·2 and mCherry-IIB-WT.

Figure S3 Still images from Video S5 focused on cytokinesis and postmitotic spreading of MEF/3T3 Tet-Off cells coexpressing EGFP-IIB-SK1·2 and mCherry-IIB-WT.

Figure S4 Localization of endogenous myosin IIA in HeLa Tet-Off cells expressing EGFP-IIB-WT or EGFP-IIB-SK1·2.

Table S1 The primers used for mutagenic PCR in this study.

Video S1 Comparison of dynamics between EGFP-IIB-SK1·2 and mCherry-IIB-WT in MRC-5 SV1 TG1 cells revealed by FRAP.

Video S2 Comparison of dynamics between mKikGR-IIB-WT and mKikGR-IIB-SK1·2 in MRC-5 SV1 TG1 cells revealed by photoconversion analysis.

Video S3 Comparison of dynamics between mKikGR-IIB-WT and mKikGR-IIB-SK1·2 in MRC-5 SV1 TG1 cells revealed by photoconversion analysis.

Video S4 Accumulation of IIB-SK1·2 in the posterior region of migrating MEF/3T3 Tet-Off cells.

Video S5 Localization of EGFP-IIB-SK1·2 and mCherry-IIB-WT in postmitotic spreading MEF/3T3 Tet-Off cells.

Additional Supporting Information may be found in the online version of this article.

Figure 1

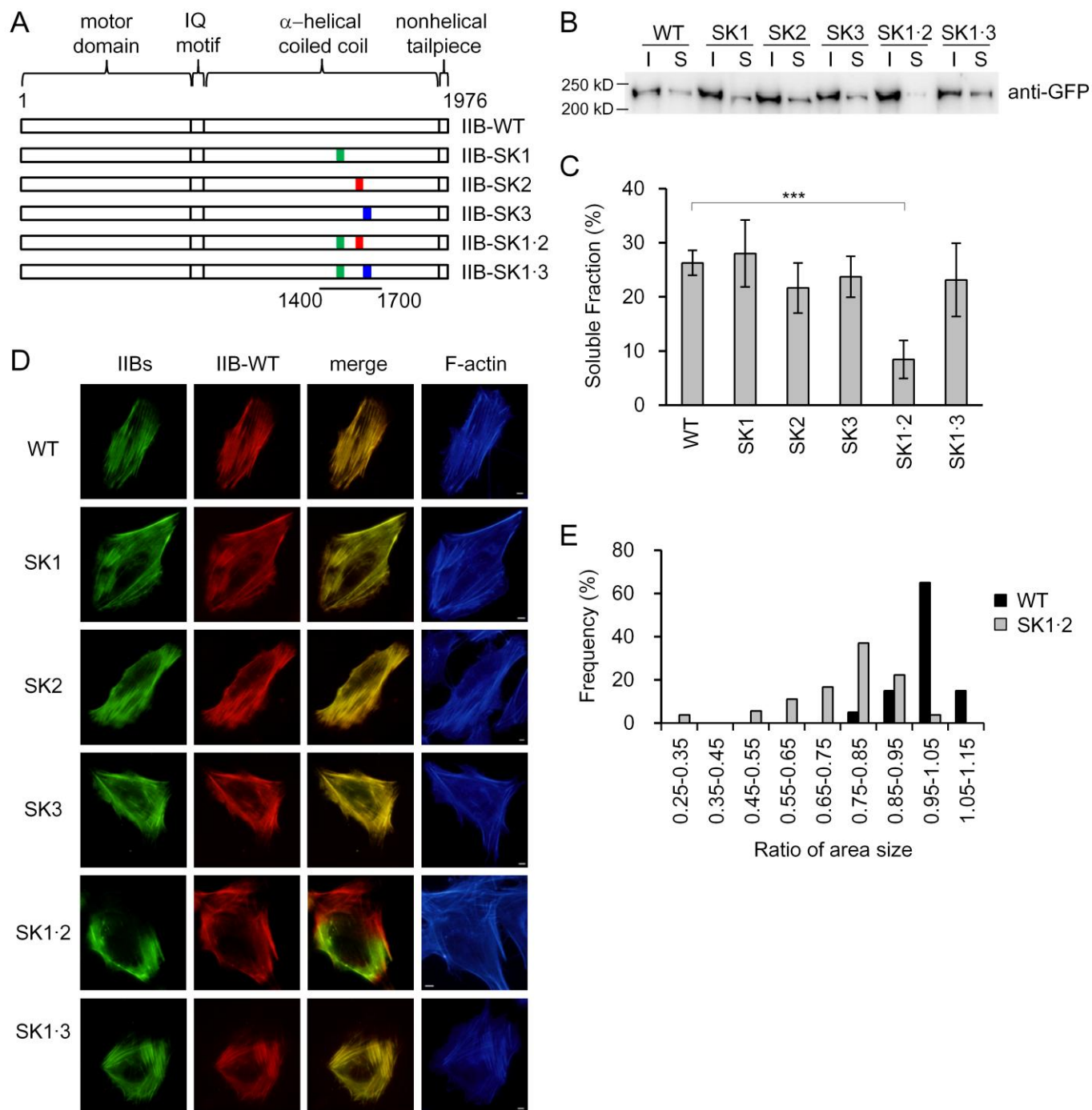


Figure 2

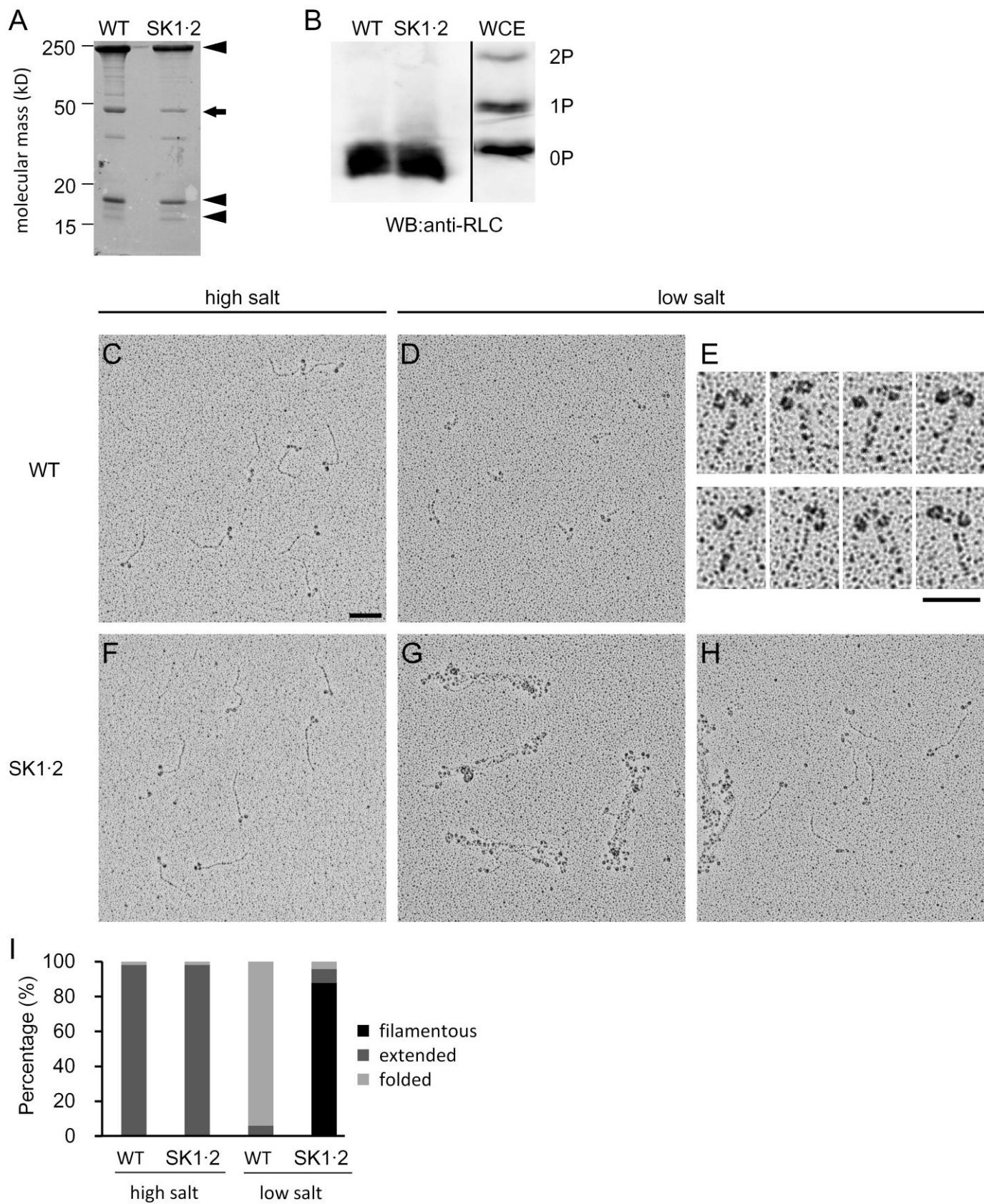


Figure 3

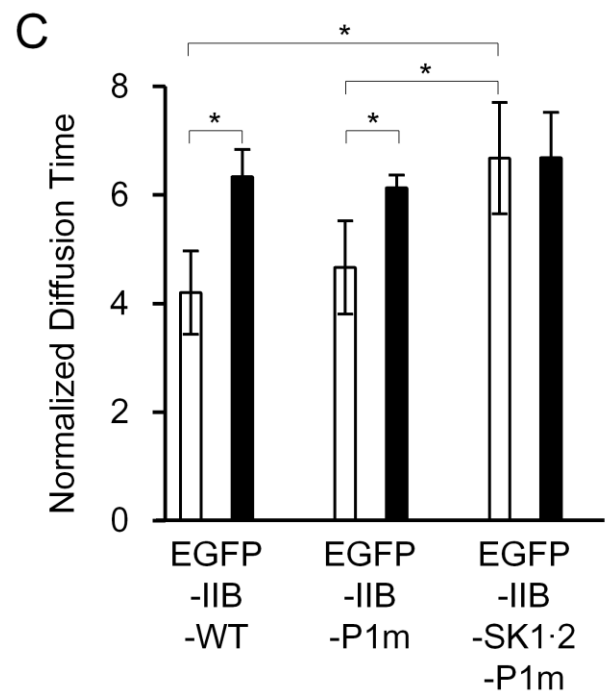
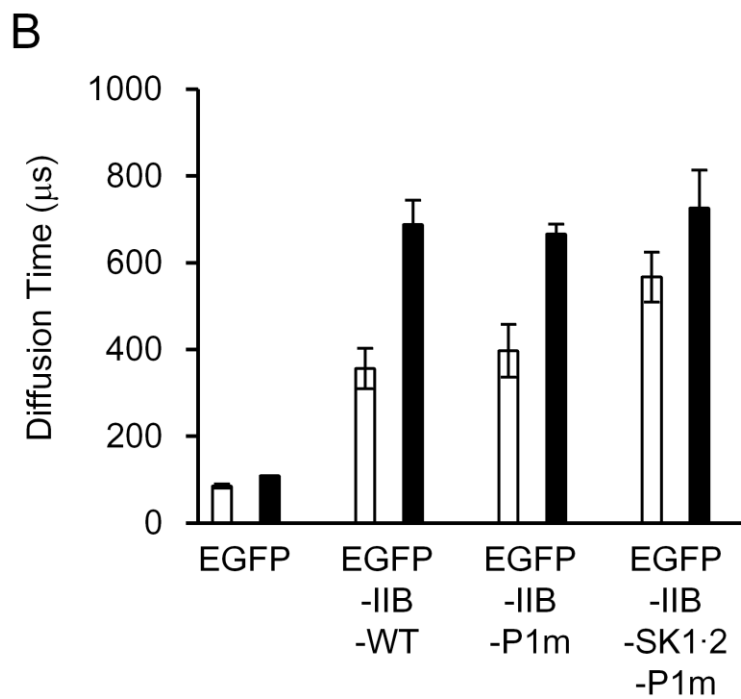
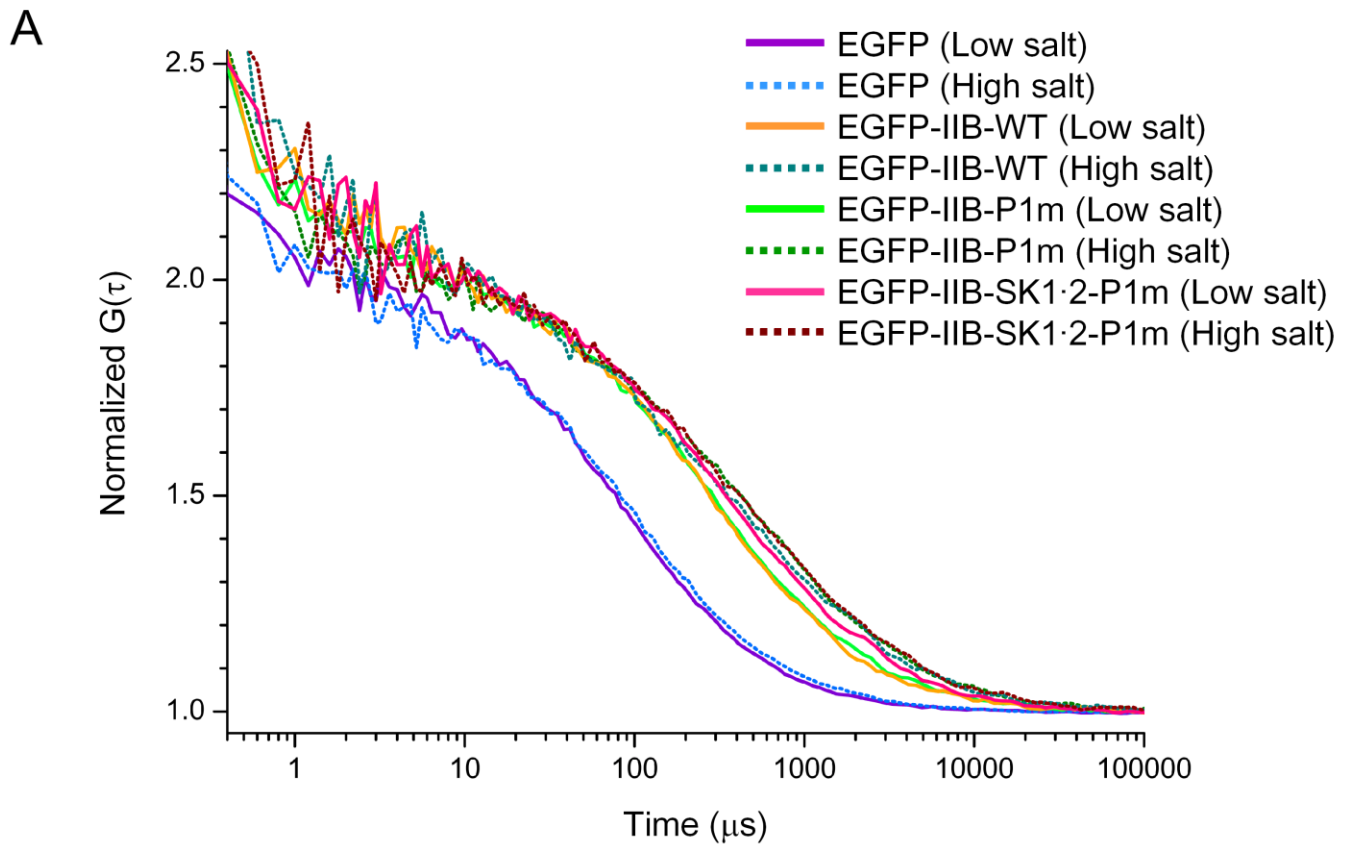


Figure 4

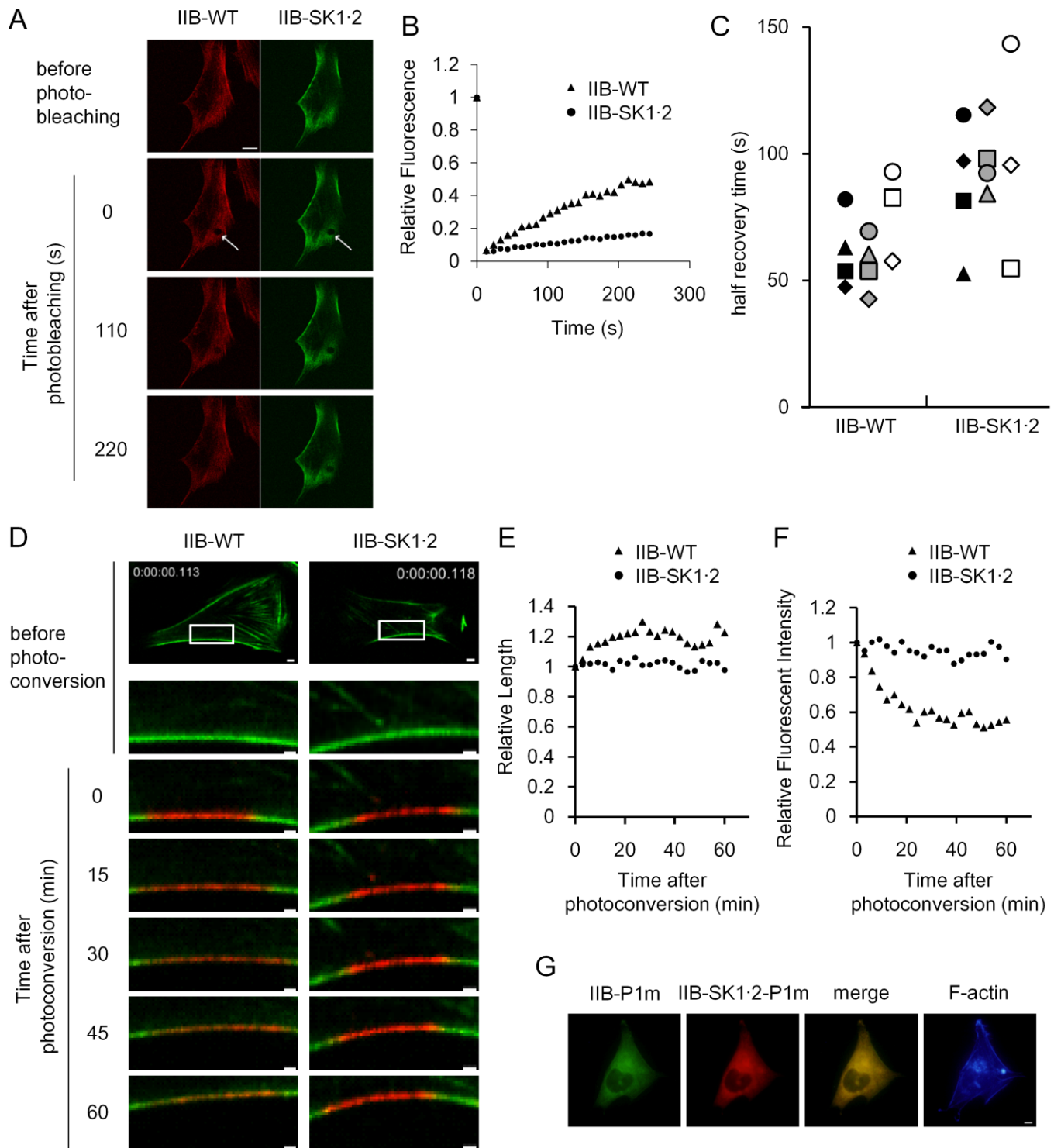


Figure 5

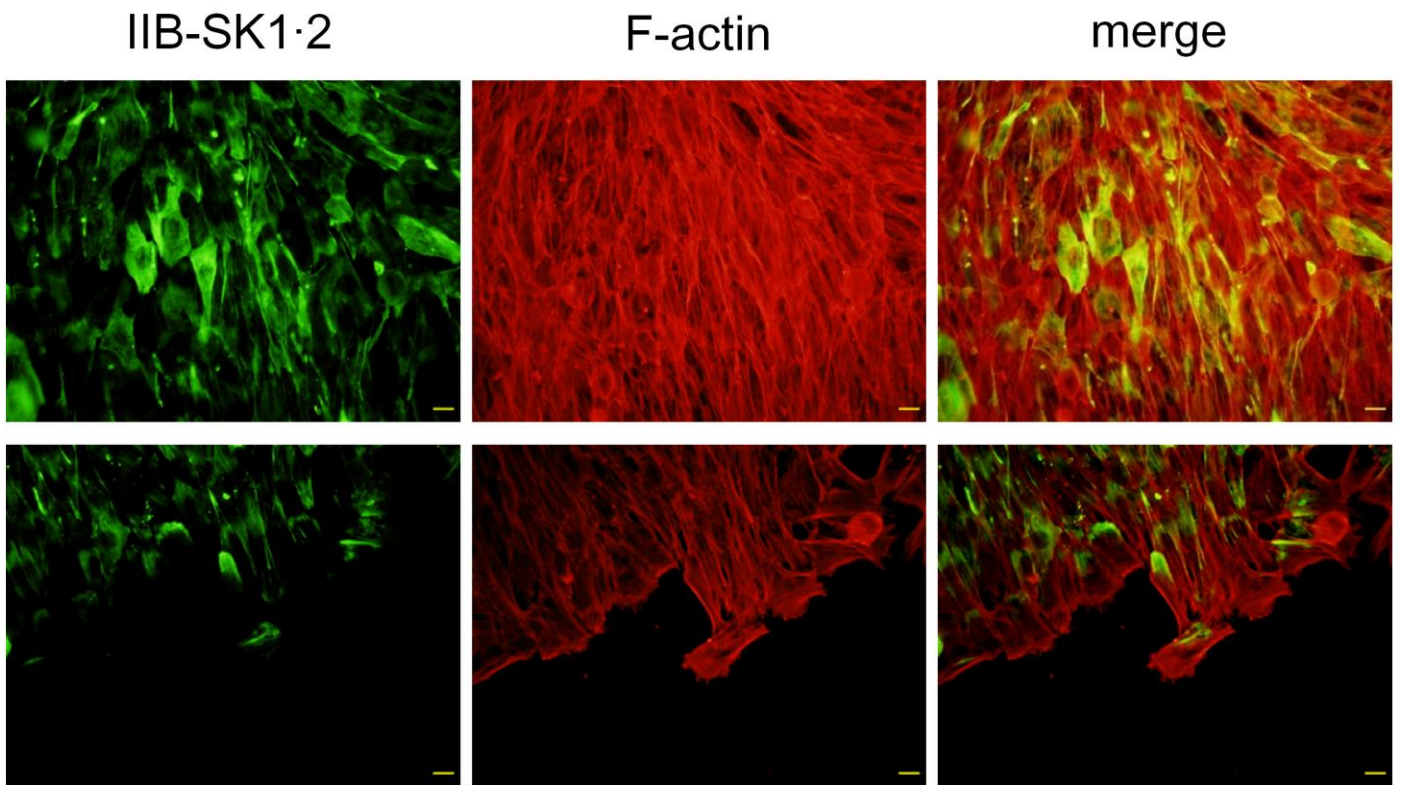


Figure 6

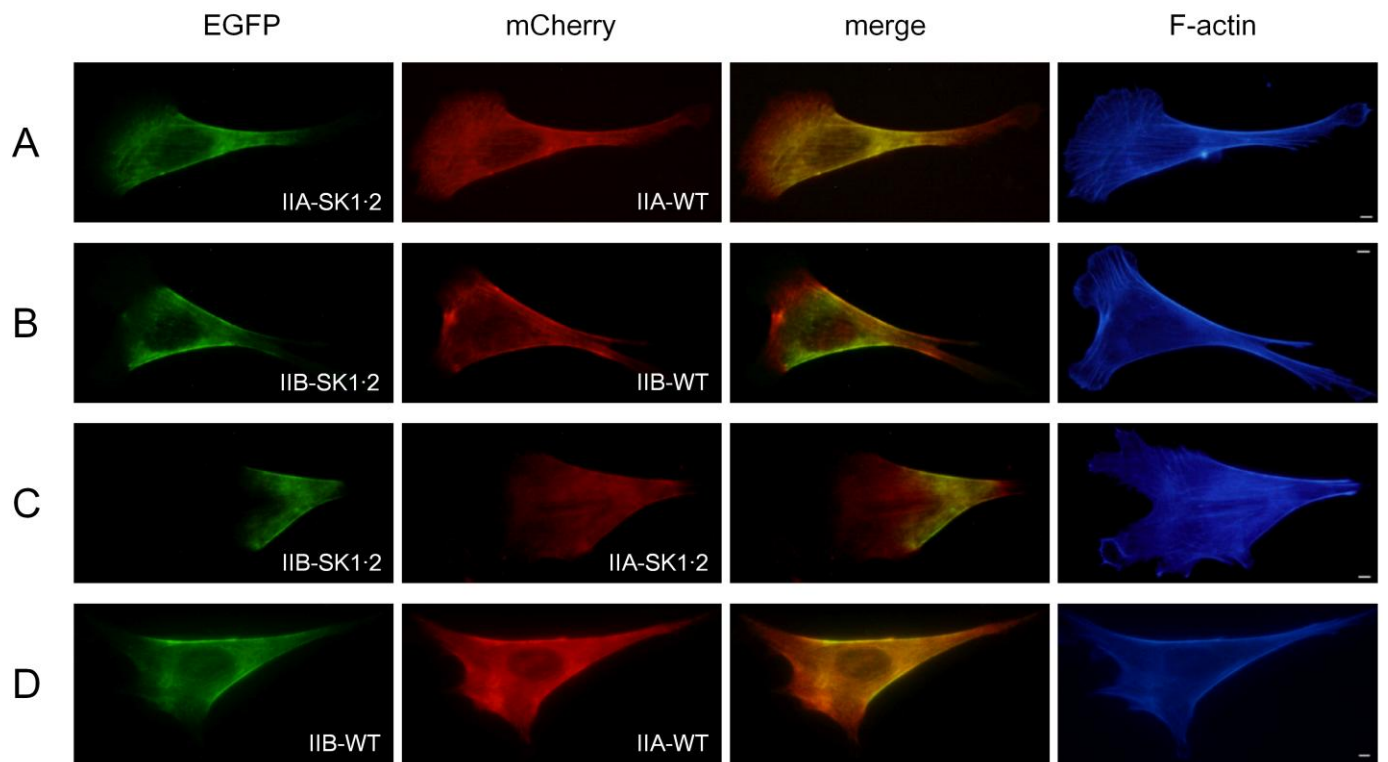


Figure 7

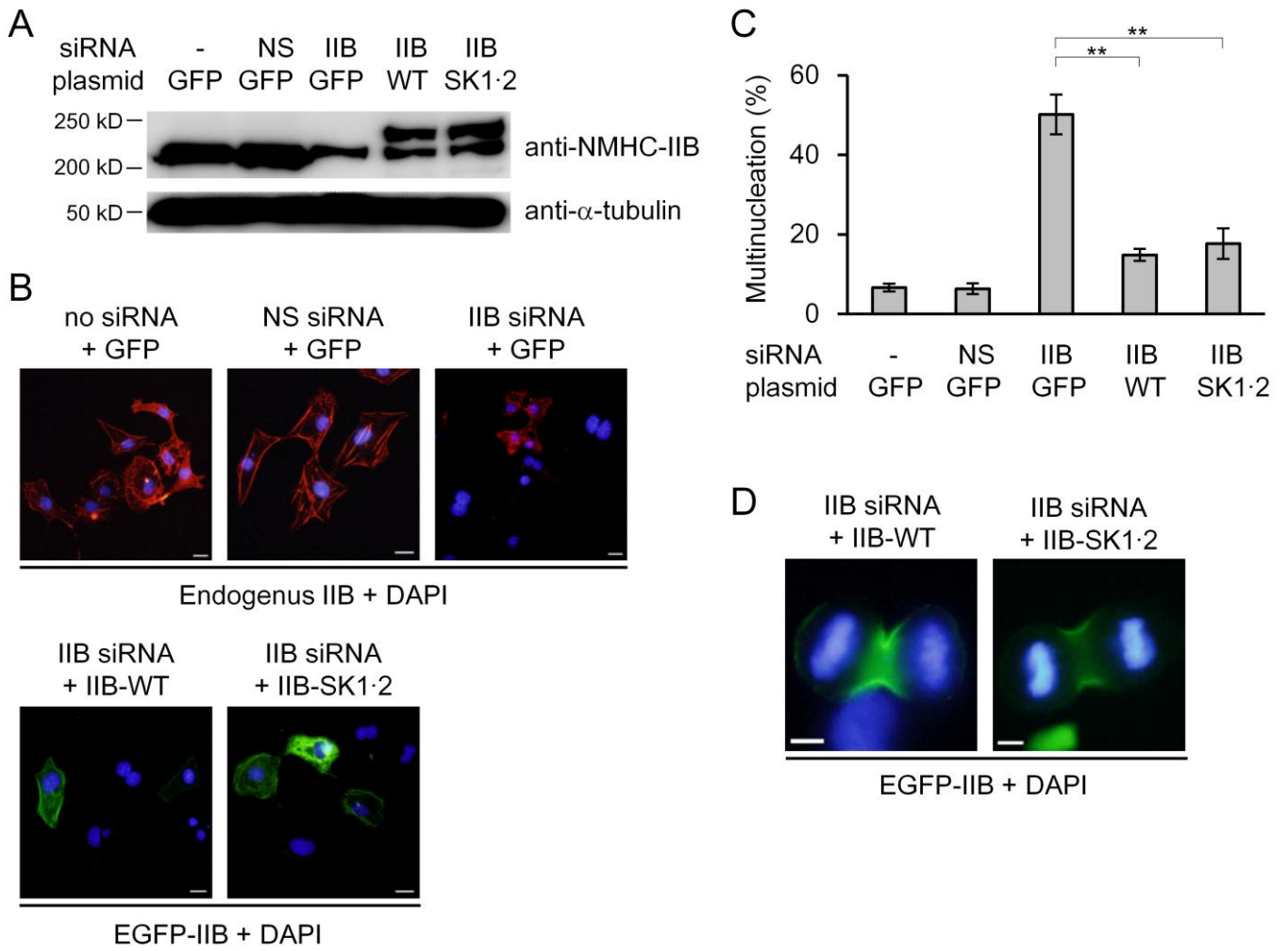
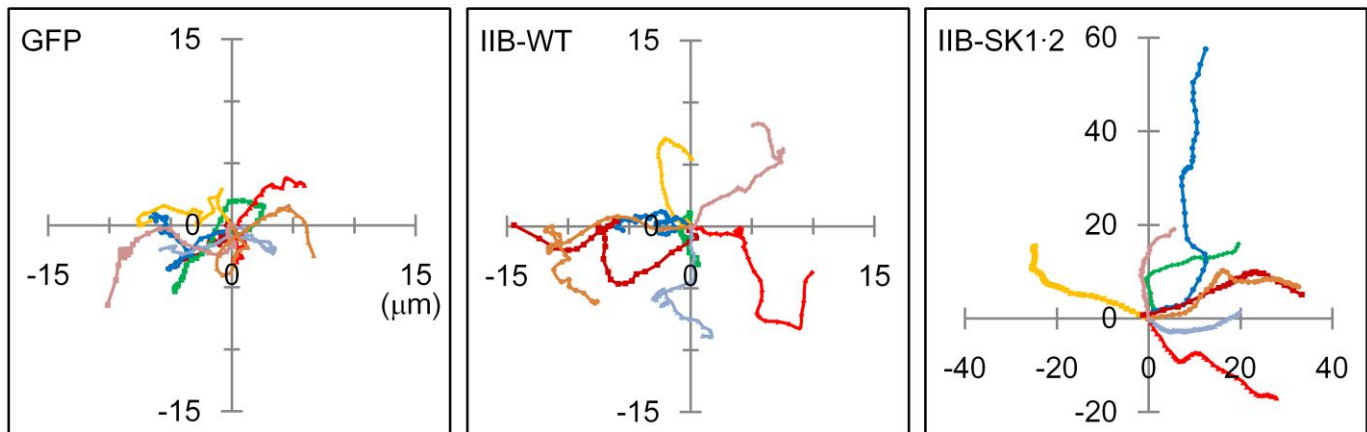
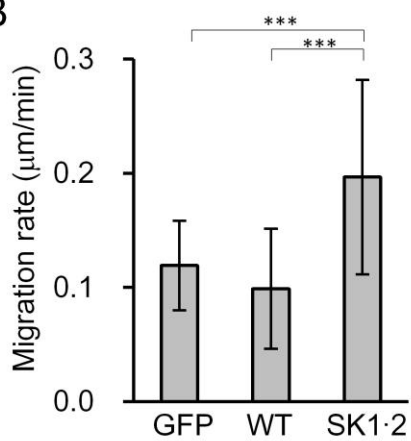


Figure 8

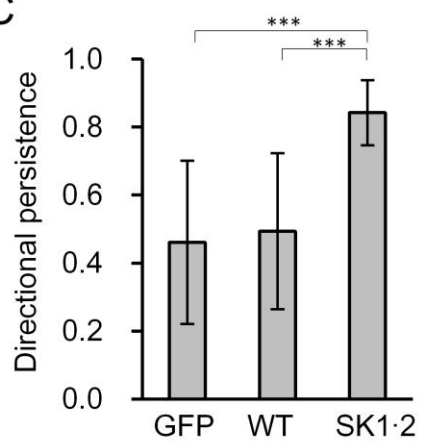
A



B



C



D

